A&A 526, A114 (2011)
DOI: 10.1051/0004-6361/201015344

Astronomy & Astrophysics

Formation and evolution of dwarf early-type galaxies in the Virgo cluster[⋆, ⋆⋆]

I. Internal kinematics

E. Toloba[1], A. Boselli[2], A. J. Cenarro[3], R. F. Peletier[4], J. Gorgas[1], A. Gil de Paz[1], and J. C. Muñoz-Mateos[1,5]

[1] Departamento de Astrofísica y CC. de la Atmósfera, Universidad Complutense de Madrid, 28040 Madrid, Spain
e-mail: [etj;jcmunoz]@astrax.fis.ucm.es, jgorgas@fis.ucm.es, gildepaz@gmail.com
[2] Laboratoire d'Astrophysique de Marseille, UMR 6110 CNRS, 38 rue F. Joliot-Curie, 13388 Marseille, France
e-mail: alessandro.boselli@oamp.fr
[3] Centro de Estudios de Física del Cosmos de Aragón, 44001 Teruel, Spain
e-mail: cenarro@cefca.es
[4] Kapteyn Astronomical Institute, Rijksuniversiteit Groningen, Postbus 800, 9700 AV Groningen, The Netherlands
e-mail: peletier@astro.rug.nl
[5] National Radio Astronomy Observatory, 520 Edgemont Road, Charlottesville, VA 22903-2475, USA

Received 6 July 2010 / Accepted 12 November 2010

ABSTRACT

We present new medium resolution kinematic data for a sample of 21 dwarf early-type galaxies (dEs) mainly in the Virgo cluster, obtained with the WHT and INT telescopes at the Roque de los Muchachos Observatory (La Palma, Spain). These data are used to study the origin of the dwarf elliptical galaxy population inhabiting clusters. We confirm that dEs are not dark matter dominated galaxies, at least not up to the half-light radius. We also find that the observed galaxies in the outer parts of the cluster are mostly rotationally supported systems with disky morphological shapes. Rotationally supported dEs have rotation curves similar to those of star-forming galaxies of similar luminosity and follow the Tully-Fisher relation. This is expected if dE galaxies are the descendants of low-luminosity star-forming systems that have recently entered the cluster environment and lost their gas due to a ram-pressure stripping event, quenching their star formation activity and transforming into quiescent systems, but conserving their angular momentum.

Key words. galaxies: clusters: individual: Virgo – galaxies: dwarf – galaxies: elliptical and lenticular, cD – galaxies: kinematics and dynamics – galaxies: evolution – galaxies: formation

1. Introduction

The processes involved in galaxy formation and evolution through cosmic time are still poorly understood. It is indeed still unclear how matter assembled to form the present-day galaxy population, whether it followed a passive evolution after the collapse of the primordial density fluctuations (secular evolution), through a subsequent merging of growing structures (hierarchical formation) or a combination of the two. A way to quantify the relative role of these different mechanisms is to study dwarf galaxies, the most numerous objects in the universe (Ferguson & Binggeli 1994). Their importance resides in the expectation that these low-luminosity systems will be the building blocks of massive galaxies in lambda cold dark matter (ΛCDM) hierarchical merging scenarios (e.g., White & Rees 1978; White & Frenk 1991).

Among dwarf galaxies, quiescent dwarfs (which we here define as all quiescent galaxies with $M_B > -18$, including both dwarf ellipticals and spheroidals, hereafter indicated as dEs) are particularly interesting since they are the most numerous population in clusters (Ferguson & Binggeli 1994). These objects were originally thought to be the low-luminosity extension of giant ellipticals (Es). Since the 1990s it has been known that dEs are composed of several families of objects (e.g. compact and low surface brightness dwarfs) (Bender et al. 1992; Kormendy et al. 2009). Later on, it was shown that dEs were no longer small Es with simple, old, and metal-poor stellar populations, but much more complex objects exhibiting a wide range of stellar contents. For example, in the Virgo cluster, they have stellar populations ranging from very young (around 1 Gyr old) luminosity-weighted ages to as old as the oldest Es galaxies (14 Gyr) (Michielsen et al. 2008). Their proximity allowed detailed studies of their structural properties that indicated that, behind their elliptical appearance, dEs show a wide variety of underlying structures, like disks, spiral arms, irregular features, etc, making them a very heterogeneous class of galaxies (Lisker et al. 2006a,b, 2007).

These proofs indicate a complex formation process shaping the evolution of dEs in clusters. Two main different processes have been proposed in the literature. The first mechanism is based on the idea that dEs are formed through internal processes, like supernova feedback, where the interstellar medium (ISM) of the progenitor star-forming galaxy is swept away by the kinetic pressure generated by supernovae (Yoshii & Arimoto 1987), although it seems highly unlikely in dark-matter dominated

---

[⋆] Appendices, Full Fig. 6, and Fig. 7 are only available in electronic form at http://www.aanda.org.

[⋆⋆] Full Table 3 is only available in electronic form at the CDS via anonymous ftp to cdsarc.u-strasbg.fr (130.79.128.5) or via http://cdsarc.u-strasbg.fr/viz-bin/qcat?J/A+A/526/A114 systems (Silich & Tenorio-Tagle 2001). The second mechanism rests upon external processes induced by the interaction with the hostile environment in which dEs reside (Sandage et al. 1985; Blanton et al. 2005). In a dense environment several mechanisms affect galaxies. This might happen through interactions with the intergalactic medium (IGM), such as ram-pressure stripping (Boselli et al. 2008a,b), galaxy-galaxy interactions (e.g., Byrd & Valtonen 1990), and galaxy harassment (e.g., Moore et al. 1998; Mastropietro et al. 2005). It has been shown that all these interactions are able to reproduce some of the observational properties of local dEs in clusters, such as their structural parameters (Lisker et al. 2006b, 2007) or their stellar populations (Geha et al. 2002, 2003; van Zee et al. 2004b; Michielsen et al. 2008; Paudel et al. 2010), but none of them have been tested against the kinematic properties. In this regard, whereas in the harassment scenario the system is rapidly heated, leading to an increase in the velocity dispersion of the galaxy and a decrease in its rotation (Mastropietro et al. 2005), the angular momentum is conserved in a ram-pressure stripping event (Boselli et al. 2008a,b).

With the aim of using kinematic data to constrain dwarf galaxy evolution, we recently started an ambitious observational programme at the Observatory El Roque de los Muchachos (La Palma, Spain) to gather medium-resolution spectroscopic data of dEs in the Virgo cluster. In this paper we present a detailed analysis of the internal kinematics focusing our attention on the most rapidly rotating systems. In Toloba et al. (2009) we studied the kinematics as a function of local environment inside the Virgo cluster. Several typical scaling relations of pressure-supported systems, such as the fundamental plane, as well as their stellar population properties, will be analysed in a forthcoming communication.

This paper is structured as follows. In Sects. 2–4 we describe the sample selection, the observations, and the data reduction process. In Sect. 5 we report on the kinematic measurements, paying special attention to the method employed and the stellar templates used. We also describe the procedure for obtaining the radial kinematic profiles (Sect. 5.1), the central velocity dispersion, and the maximum rotational speed of the selected galaxies (Sect. 5.2), allowing comparisons with previous works (Sect. 5.3). Combined with photometric data (Sect. 6), the present kinematic observations are used to study the properties of rotationally supported systems in the framework of various models of galaxy evolution (Sects. 7–9).

2. The sample

The sample analysed in this work is composed of galaxies with $M_r > -16$ classified as dE or dS0 in the Virgo Cluster Catalog (VCC) by Binggeli et al. (1985). All galaxies have been selected to have SDSS imaging and to be within the GALEX MIS fields (Boselli et al. 2005), thus to have a measured UV magnitude or an upper limit. To these we added a few field-quiescent dwarfs (originally used as fillers in our observing runs) useful for comparison in a statistical study. Out of the 43 Virgo galaxies satisfying these requirements in the VCC, 18 have been observed for this work. To make the observations accessible to 2.5–4.2 m telescopes, we chose those objects with the highest surface brightness.

The field sample consists of early-type dwarfs in low-density regions with magnitudes between $-18.5 < M_r < -14.5$ and distances similar to Virgo (375 km s^{-1} $< v <$ 1875 km s^{-1}, 5–25 Mpc). Quiescent objects were selected assuming the colour criterion FUV-NUV > 0.9 or $u - g > 1.2$ when UV detections were not available. We observed only 3 out of 10 field dEs candidates. To these 18 Virgo and three field dEs we added M 32, selected to test the setup of the instruments. Thanks to the large amount of available data, M 32 is also an ideal target for comparison with other data available in the literature.

Although we can consider it representative of the bright end of the Virgo Cluster dE population, the observed sample is not complete in any sense.

3. Observations

The observing time that we obtained for this work was part of the International Time Program (ITP 2005–2007) at El Roque de los Muchachos Observatory. Here we focus on the medium-resolution ($R \simeq 3800$), long-slit spectroscopy carried out during three observing runs. In Runs 1 and 3 (December 2005, February 2007) we used the ISIS double-arm spectrograph at the 4.2 m WHT, and in Run 2 (January 2007) we used the IDS spectrograph at the INT (2.5 m telescope).

The advantage of ISIS over IDS is that it allows us to use a dichroic (*5300 dichroic* in our case) to split the light into two beams to observe two wavelength ranges simultaneously, one in the blue optical part of the spectra and another in the red. This technique allowed us to cover, in three settings in the first run, the full wavelength range from 3500 Å to 8950 Å, using a mirror to cover 5000–5600 Å, the only range that we could not cover with this dichroic. In the third run we used two settings to cover the same wavelength range except for the dichroic gap.

The wavelength range covered by the IDS was smaller (4600–5960 Å), since detector and grating are the same as on the blue arm of ISIS, the data obtained had similar resolution. The spectral resolution ($R \simeq 3800$) is high enough to obtain reliable kinematics for dwarf galaxies. All the details of the configurations used in each run are specified in Table 1.

In Table 2 we list the observed sample. Column 5 presents the morphological type classification according to Lisker et al. (2006a) and Lisker et al. (2006b): dE(di) indicates dwarf ellipticals with a certain, probable or possible underlying disk (i.e. showing spiral arms, edge-on disks, and/or a bar) or other structures (such as irregular central features (VCC21)); dE(bc) refers to galaxies with a blue centre; dE to galaxies with no evident underlying structure. Four out of our 21 dwarf galaxies were not in the Lisker et al. sample (NGC 3073, PGC1007217, PGC1154903 and VCC1947), therefore we classified them as described in Section 6, attending only to their boxyness/diskyness. Column 6 gives the Virgo substructure to which the galaxy belongs, taken from the GOLDMine Database (Gavazzi et al. 2003) and defined as in Gavazzi et al. (1999). Columns 7 and 8 refer to the observational campaign (see Table 1) and the exposure time for each setting, which allowed us to get a typical signal-to-noise ratio[1] for the central spectra of ~60 Å^{-1}, enough to obtain reliable central kinematics. The galaxies were observed along their major axis. Their position angles (PA) from the HyperLEDA Database (Paturel et al. 2003) are given in Col. 9. Column 10 gives the Galactic colour excess from Schlegel et al. (1998).

A total of 37 B to M stars in common with the MILES library (Sánchez-Blázquez et al. 2006) and the CaT library (Cenarro et al. 2001) were observed to flux-calibrate our data and to use them as templates for velocity dispersion measurements.

---

[1] The S/N per Å^{-1} is obtained dividing the S/N per pixel by the square root of the spatial scale along the slit. This measurement is therefore independent of the instrument used.

Table 1. Observational configurations.

	Run 1		Run 2	Run 3	
Date	Dec. 24-27 2005		Jan. 21–23 2007	Feb. 10–12 2007	
Telescope	WHT 4.2 m		INT 2.5 m	WHT 4.2	
Spectrograph	ISIS		IDS	ISIS	
Detector	EEV12(blue)	Marconi(red)	EEV10	EEV12(blue)	RedPlus(red)
Grating	R1200B(blue)	R600R (red)	R1200B	R1200B(blue)	R600R(red)
Wavelength range 1 (Å)	3500–4300	5500–6700	3700–4790	3500–4300	5500–6700
Wavelength range 2 (Å)	4100–4900	7750–8950	4600–5690	4100–4900	7750–8950
Wavelength range 3 (Å)	4800–5600	–	–	–	–
Dispersion (Å/pixel)	0.44	0.87	0.48	0.44	0.97
Spectral resolution (*FWHM*, Å)	1.56	3.22	1.80	1.56	3.23
Instrumental resolution (km s^{-1})	40	58	46	40	58
Spatial scale (″/pix)	0.40	0.44	0.40	0.40	0.44
Slit width (″)	1.95	1.95	1.94	1.91	1.91

Table 2. The observed galaxies.

Galaxy	Other name	RA(J2000) (h:m:s)	Dec(J2000) (°:′:″)	Type	Env.	Run	$t_{\rm exp}$ (s)	PA (°)	$E(B-V)$ (mag)
M 32	NGC 221	00:42:41.84	+40:51:57.4	cE2	M31 group	1	1350	170	0.062
NGC 3073	UGC 05374	10:00:52.10	+55:37:08.0	dE(di)	Field	1	3200	120	0.010
PGC 1007217	2MASX J02413514-0810243	02:41:35.8	–08:10:24.8	dE(di)	Field	1	3600	126	0.024
PGC 1154903	2MASX J02420036+0000531	02:42:00.3	+00:00:52.3	dE	Field	1	3600	126	0.031
VCC 21	IC 3025	12:10:23.14	+10:11:18.9	dE(di,bc)	Virgo N Cloud	2	3600	99	0.021
VCC 308	IC 3131	12:18:50.77	+07:51:41.3	dE(di,bc)	Virgo B Cluster	3	2400	109	0.021
VCC 397	CGCG 042-031	12:20:12.25	+06:37:23.6	dE(di)	Virgo B Cluster	3	3600	133	0.020
VCC 523	NGC 4306	12:22:04.13	+12:47:15.1	dE(di)	Virgo A Cluster	1	3400	144	0.044
VCC 856	IC 3328	12:25:57.93	+10:03:13.8	dE(di)	Virgo B Cluster	2	2740	72	0.024
VCC 917	IC 3344	12:26:32.40	+13:34:43.8	dE	Virgo A Cluster	3	3600	57	0.032
VCC 990	IC 3369	12:27:16.91	+16:01:28.4	dE(di)	Virgo A Cluster	2	3000	135	0.028
VCC 1087	IC 3381	12:28:17.88	+11:47:23.7	dE	Virgo A Cluster	3	3600	106	0.026
VCC 1122	IC 3393	12:28:41.74	+12:54:57.3	dE	Virgo A Cluster	3	3600	132	0.021
VCC 1183	IC 3413	12:29:22.49	+11:26:01.8	dE(di)	Virgo A Cluster	2	3600	144	0.031
VCC 1261	NGC 4482	12:30:10.35	+10:46:46.3	dE	Virgo A Cluster	2	6930	133	0.028
VCC 1431	IC 3470	12:32:23.39	+11:15:47.4	dE	Virgo A Cluster	2	3000	135	0.054
VCC 1549	IC 3510	12:34:14.85	+11:04:18.1	dE	Virgo A Cluster	2	3300	13	0.030
VCC 1695	IC 3586	12:36:54.79	+12:31:12.3	dE(di)	Virgo A Cluster	3	3600	39	0.045
VCC 1861	IC 3652	12:40:58.60	+11:11:04.1	dE	Virgo E Cloud	3	3600	109	0.030
VCC 1910	IC 809	12:42:08.68	+11:45:15.9	dE(di)	Virgo E Cloud	2	3800	135	0.030
VCC 1912	IC 810	12:42:09.12	+12:35:48.8	dE(bc)	Virgo E Cloud	2	3600	166	0.032
VCC 1947	CGCG 043-003	12:42:56.36	+03:40:35.6	dE(di)	Virgo S Cloud	2	3060	126	0.027

4. Data reduction

The data reduction was performed with $\mathrm{R_ED^{uc}_mE}$ (Cardiel 1999), a package specially designed to reduce long-slit spectroscopy with particular attention to the treatment of errors. This package is ideal for treating the data and error frames in parallel, producing an error spectrum associated with each individual data spectrum, which means that the errors are controlled at all times.

Thanks to the similar instrumental configurations used on all observing runs, the reduction process for both telescopes was the same. The standard procedure for long-slit spectroscopy data reduction consists of bias and dark current subtraction, flat-fielding (using observations of tungsten lamps and twilight sky to correct for high and low frequency variations respectively), cosmic ray cleaning, C-distortion correction, wavelength calibration, S-distortion correction, sky subtraction, atmospheric and interstellar extinction correction, and flux calibration. We give below some comments on particularly important steps.

Flat-fielding. The flat-fielding correction is a delicate step at the near infrared due to the fringing patterns. In the first run, the Marconi CCD suffered from significant fringing that varied with the telescope position. Since complete removal of the fringing in run 1 was not possible, we did not use the red Marconi-CCD data to determine the galaxy kinematics. The fringing produced by RedPlus, the new CCD optimised to avoid these patterns, was much lower with an amplitude of only ∼1% independent of position.

Wavelength calibration. The wavelength calibration was performed using between 65 and 100 arc lines depending on the instrumental configuration. They were fitted with a fifth-order polynomial that led to a typical RMS dispersion of 0.1–0.25 Å.

S-distortion, alignment of the spectra. During the spectroscopic observations, the galaxies were not perfectly aligned with the rows of the detector. This effect is crucial when measuring gradients of any type (rotation curves, velocity dispersion profiles, or line-strength indices). This effect was corrected using a routine that found the position of the galaxy centre as a function of wavelength, fitted all these positions with a low-order polynomial, and straightened the spectra using that polynomial. This alignment was done with a technique that minimised the errors caused by the discretization of the signal. This technique consists of adopting a more realistic distribution of the light in each pixel than when just assuming it to be constant. To achieve this, the signal in each pixel is fitted with a second-order polynomial using the available information in the adjacent pixels.

Sky subtraction. Sky subtraction is critical for studies where the spectra are analysed at light levels corresponding to only a few percent of the sky signal, as in our case. For each galaxy observation, a sky image was generated fitting the data at each wavelength with a first-order polynomial in regions on both sides of the galaxy close to the ends of the slit (which has a length of 3.7 arcmin on the WHT and 3.3 arcmin on the INT). This was possible since for all targets except M 32 the galaxy filled only a small region of the slit, so this synthetic sky image was free of contamination from the galaxy. For M 32, we observed a separate sky frame moving the telescope from the coordinates of the galaxy to a position $\Delta\alpha = -416''$ (West), $\Delta\delta = -459''$ (South) far enough from M 32 to avoid its light but with the same level of contamination from M 31.

Extinction correction. Atmospheric extinction was calculated using the extinction curve for El Roque de los Muchachos Observatory (`www.ing.iac.es/Astronomy/observing/manuals/ps/tech_notes/tn031.pdf`). The Galactic extinction was corrected using the curve of Fitzpatrick (1999) and the reddening from Schlegel et al. (1998) listed in Table 2.

Flux calibration. The spectra was calibrated in relative flux using the observed stars in common with the MILES library (Sánchez-Blázquez et al. 2006) for the optical spectra and with the CaT library (Cenarro et al. 2001) for the near infrared. For each observed star we obtained a flux-calibration curve. All of them were averaged to obtain one unique flux curve for each run and instrumental configuration. The deviations in each flux-calibration curve from the averaged one were introduced as uncertainties in the error spectra. The typical deviation was about 2% reaching ~7% in the first and last ~150 Å of each setup spectra where the noise is the highest.

5. Measurement of the kinematic parameters

The stellar kinematics of galaxies (radial velocities and velocity dispersions) were calculated using the routine MOVEL included in RED$^{\rm uc}_{\rm m}$E package (Cardiel 1999). This routine is based on the Fourier quotient method described by Sargent & Turner (1977) and refined with the OPTEMA algorithm (González 1993), which allows us to overcome the typical template mismatch problem. In order to do this, a number of stars of different spectral types and luminosity classes were introduced in the programme to create a model galaxy. These stars were of spectral type B9, A0, A3V, G0, G2III, G5III, G8III, G9III, K0III, K0I, K2III, K3III, M0III, and M2III. The model galaxy was created and processed in parallel with the galaxy spectrum. To build the model galaxy, all the template spectra were scaled, shifted, and broadened according to a first guess of γ (mean line-strength), v (radial velocity), and σ (velocity dispersion). Then the algorithm looked for the linear combination of these template stars that matched the observed galaxy spectrum best. The best linear combination of observed stars was chosen as the one that minimises the residuals between the galaxy spectrum and the broadened optimal template. This provided a first model galaxy with a first kinematic output (γ, v and σ). This model galaxy was then improved using this new guess of kinematic parameters. The process was iterated until it converged. The emission lines, found only for the field dwarf galaxies, and some large sky line residuals, only present in some cases, were masked, so that the programme did not use them for minimising the residuals.

To minimise template mismatch effects, it is essential to use a variety of spectral types and luminosity classes as templates, which are representative of the stellar population of the observed galaxy. As we discuss in Sect. 5.3.1, small differences in ages and metallicities could lead to a partial fit of the strongest lines and therefore affect the derived velocity dispersion of the galaxy.

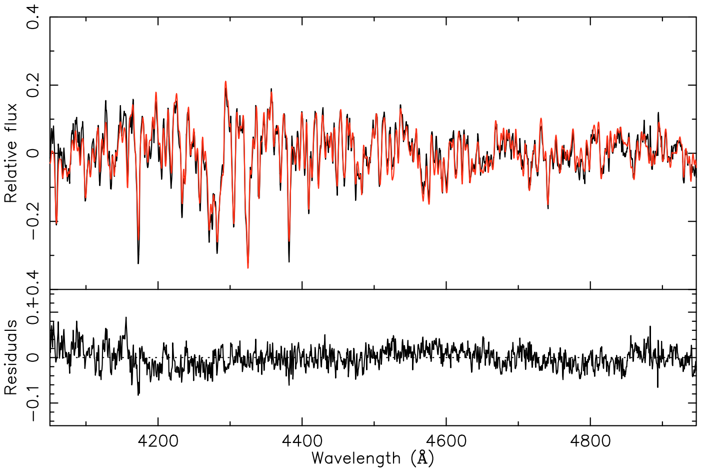

Fig. 1. Example of the fit computed by MOVEL. *Upper panel*: in black, the central spectrum of VCC523. The spectrum has been continuum-subtracted and normalised. The optimal template that fits the galaxy is shown in red, a linear combination with different weights of the stars observed with the same configuration as the galaxy. *Bottom panel*: residuals of the galaxy-composite template fit.

It is also important to check whether the observed stars were filling the slit during the observation. If they were not, the instrumental profile would not affect them in the same way as in the galaxies, and as a consequence, the σ that one would measure for the galaxy would be $\sqrt{\sigma^2_{\rm inst} + \sigma^2_{\rm gal}}$, where $\sigma_{\rm gal}$ is the intrinsic velocity dispersion of the galaxy and $\sigma_{\rm inst}$, in this case, is the quadratic instrumental difference between the galaxies and the stars.

To correct for this effect, the physical slit width[2] is required. We calculated it from the spatial scale and the *FWHM* (in pixels) of the arc lines, which illuminate the slit homogeneously. To see whether the stars were filling the slit completely, we checked that the *FWHM* of their spatial profile was larger than the physical slit width. If this was not the case, the spatial profile of the star was broadened accordingly. Although this introduced some uncertainties, the data quality improved by making this correction. The value of σ measured and adopted in this work is thus the intrinsic velocity dispersion of the galaxy corrected for possible instrumental effects.

Figure 1 shows a typical fit of the observed central spectral of a galaxy and the corresponding optimal template broadened with a Gaussian with the derived dynamical parameters. The errors in velocity and σ were computed through Monte-Carlo simulations, then by repeating the whole process (including the derivation of the optimal template) for 100 simulated galaxy spectra created using the error spectra obtained during the reduction process. The observed and simulated spectra match perfectly.

5.1. Kinematic parameter profiles

To measure kinematic gradients it is important to determine the minimum S/N needed to measure reliable radial velocities and velocity dispersions. To do that, we designed and carried out a

---

[2] During the observation, an indicative width of the slit is selected by the user through a web interface.

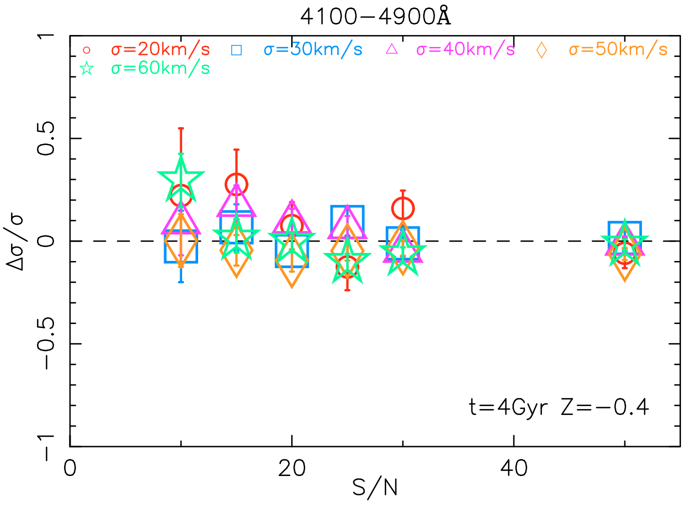

Fig. 2. Simulations to study the minimum S/N to obtain reliable measurements of the velocity dispersion, plotting $\Delta\sigma/\sigma$ (defined as $(\sigma_{\rm o} - \sigma_{\rm i})/\sigma_{\rm i}$), the relative error introduced when measuring the σ of a galaxy as a function of S/N. Different colours show different σ for the simulated galaxies and it assumes a stellar population of 4 Gyr and $Z = -0.4$.

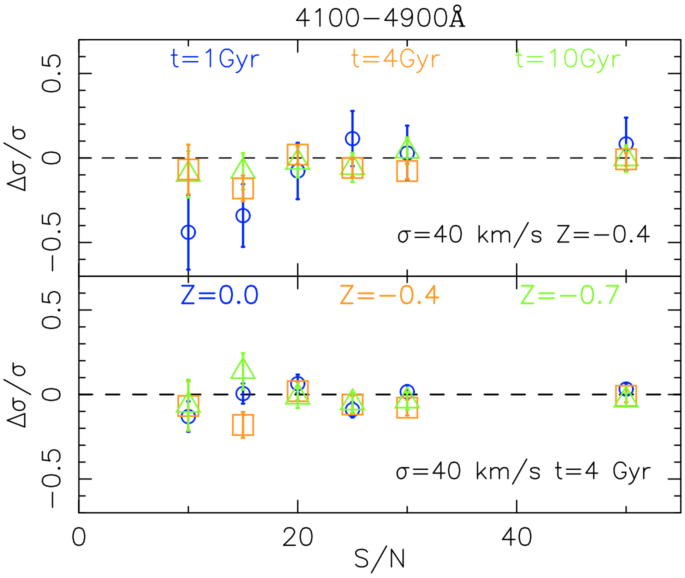

Fig. 3. Simulations to study the dependence of the stellar population of the galaxy on the measurement of its velocity dispersion. We plot the relative offsets found between the measured σ and the velocity dispersion introduced in the simulated galaxy as a function of the S/N. In both panels a typical σ of 40 km s^{-1} has been considered. In the upper panel we fix the metallicity of the galaxy to −0.4 and study the influence of the age on the velocity dispersion. In the lower panel the parameter fixed is the age to 4 Gyr to analyse the influence of the metallicity on σ.

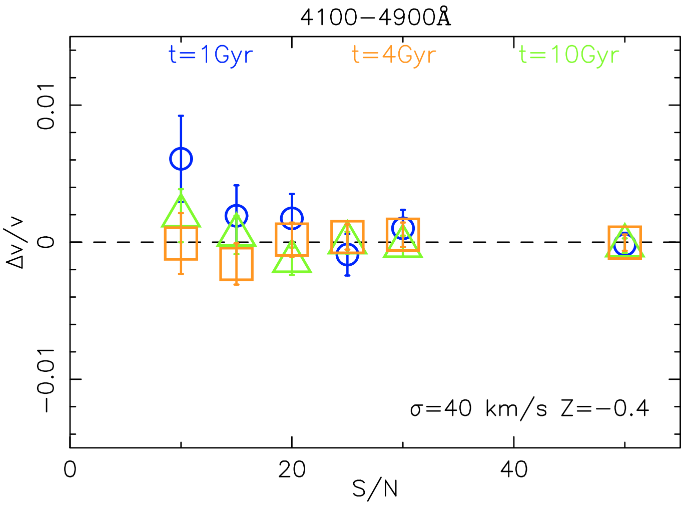

Fig. 4. Simulations to study the influence of the stellar populations and the S/N on the measurement of the radial velocities. We plot the relative uncertainty when measuring the radial velocities $\Delta v/v$, defined as $(v_{\rm o} - v_{\rm i})/v_{\rm i}$) as a function of the S/N. Only the results for the radial velocity v = 1500 km s^{-1} are shown because the offsets and errors found are independent of the radial velocity of the galaxy. The results plotted are for a typical dwarf galaxy with velocity dispersion of 40 km s^{-1} and metallicity −0.4. The velocity dispersion does not have any effect on either the measurement of radial velocities or the metallicities. Note the different scale in the y-axis compared to Figs. 2 and 3.

test exercise based on Monte-Carlo simulations that constraints the errors and systematic effects in the measurement of radial velocities and velocity dispersions on fake galaxy spectra with known input kinematic parameters and different ages, metallicities, and S/N. This can be outlined in the following steps.

i) From the simple stellar population models from PEGASE.HR (*FWHM* ∼ 0.55 Å; Le Borgne et al. 2004) we selected a subset of 9 model spectra (3 ages and 3 metallicities) representative of quiescent dwarf galaxies: ages of 1 Gyr, 4 Gyr, 10 Gyr; metallicities of $Z = 0.0$, $Z = -0.4$, $Z = -0.7$. The spectral resolution of these models are needed since in our bluer configuration the resolution is ∼1.6 Å.

ii) Considering our instrumental resolution, each model was broadened and redshifted to match a set of input velocity dispersions, $\sigma_{\rm i}$, (9 values between 20 km s^{-1} and 60 km s^{-1} in steps of 5 km s^{-1}) and radial velocities, $v_{\rm i}$, (800 km s^{-1} and 1500 km s^{-1}, typical values of Virgo cluster members). This amounts a total of 162 model spectra.

iii) For each one of the above spectra we added different levels of random noise to match S/N of 10, 15, 20, 25, 30, and 50, hence ending up with 972 model galaxy spectra.

iv) For each simulated galaxy spectrum we run exactly the same MOVEL procedure as we did for our dE galaxy sample, using the same template stars and MOVEL parameters. One hundred Monte-Carlo simulations for each model galaxy were carried out to get reliable errors of the derived kinematic parameters, $\sigma_{\rm o}$ and $v_{\rm o}$, obtained as the mean value of the 100 Monte-Carlo simulations in each case. Since the input kinematics $\sigma_{\rm i}$ and $v_{\rm i}$ are set by construction, comparisons and reliability analysis are immediately performed.

The above procedure was carried out for each instrumental configuration in each of the 5 different spectral regions. The results obtained are shown in Figs. 2–4.

After correcting for any systematic offsets in radial velocity and velocity dispersion caused by small intrinsic differences between PEGASE.HR models and our observed stars, we analysed the simulations looking at the relative differences between the measured values and the parameters introduced in the simulated galaxies ($\Delta v/v = (v_{\rm o}-v_{\rm i})/v_{\rm i}$ and $\Delta\sigma/\sigma = \sigma_{\rm o}-\sigma_{\rm i})/\sigma_{\rm i}$). Figures 2–4 show these differences as a function of S/N in the wavelength range 4100–4900 Å, a range shared by the WHT and INT observations where lines as important as the G-band are located. The

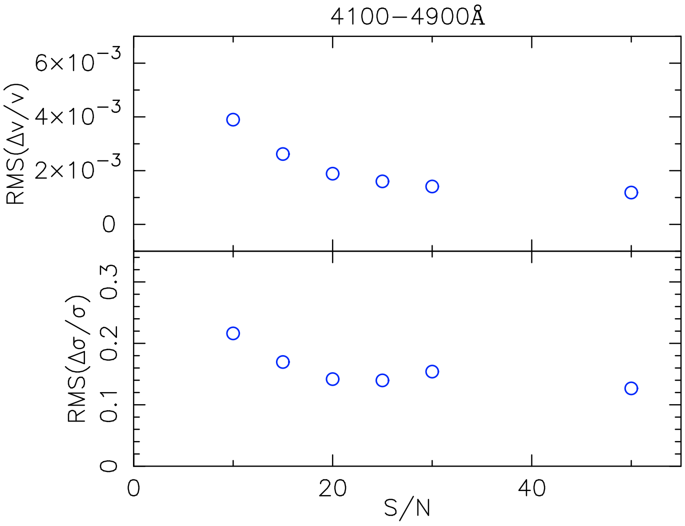

Fig. 5. Total scatter in the differences found for the 972 simulations computed as a function of the S/N. In this figure all models for all stellar populations and velocity dispersion parameters have been used.

error bars in these three figures show the relative uncertainties obtained by MOVEL as the RMS scatter resulting from the 100 Monte-Carlo simulations for each model galaxy.

In Fig. 2 we study the influence of the S/N and the instrumental resolution on the measurement of the velocity dispersion of a galaxy. Each point represents a galaxy with similar stellar populations (age 4 Gyr and metallicity −0.4) but different velocity dispersions (from 20 to 60 km s^{-1}). As expected, the errors increase dramatically at the lowest S/N. For low S/N ($S/N = 10$) offsets are found even for galaxies with high σ's, so the velocity dispersions derived at this S/N cannot be trusted. In contrast, for S/N higher than or equal to 15 we do not find statistically significant offsets, with the exception of measurements below half the instrumental resolution ($\sigma = 20$ km s^{-1}) where special care must be taken. Only for S/N higher than 20 the measured σ can be fully trusted for velocity dispersions as low as half the instrumental resolution.

Figure 3 presents the influence of the stellar populations on the measurement of the velocity dispersion of a galaxy. In the upper panel we show the effect of the age on a dwarf galaxy of $\sigma = 40$ km s^{-1} and $Z = -0.4$, while in the lower panel we show the effect of the metallicity for a galaxy with $\sigma = 40$ km s^{-1} and 4 Gyr old. In this case, although the errors barely depend on metallicity, the age-dependence is crucial, and for populations as young as 1 Gyr the σ measurements are underestimated for a S/N below 15.

In Fig. 4 we analyse the effect of the stellar populations on the computation of the radial velocity. A change in neither the velocity dispersion nor the metallicity have appreciable effects on this variable. Only the age of the stellar population influences the determination of the radial velocity whenever the age is young, around 1 Gyr. The uncertainty induced by age variations, however, is small, $\leq 1\%$, thus rotation velocities can be measured accurately down to $S/N \sim 10$.

In Fig. 5 we plot the expected RMS error (i.e. RMS of the average of all the simulations) as a function of S/N to have a statistical estimate of the uncertainty. The average of all the simulations (corresponding to different velocity dispersions, ages, and metallicities) for each S/N, takes into account that for a target galaxy we do not have a priori information about either its velocity dispersion or the parameters of the stellar population.

Table 3. Kinematic profiles for VCC990.

R_v ($''$)	v (km s^{-1})	R_σ ($''$)	σ (km s^{-1})
–5.43	1.8 ± 5.5	–4.98	36.0 ± 6.2
–3.56	16.8± 6.4	–2.36	47.2 ± 6.0
–2.58	9.8± 6.3	–1.38	39.2 ± 5.4
–2.00	10.5± 6.4	–0.80	35.8 ± 4.6
–1.60	1.7± 6.2	–0.40	32.5 ± 3.5
–1.20	–6.3± 4.4	0.00	42.2 ± 3.1
–0.80	3.9 ± 2.7	0.40	41.3 ± 2.8
–0.40	0.1 ± 2.3	0.80	39.7 ± 3.6
0.00	6.8 ± 2.0	1.38	37.7 ± 3.9
0.40	2.2 ± 2.4	2.36	36.1 ± 8.5
0.80	1.0 ± 3.1	4.97	37.4 ± 5.6
1.20	–5.2± 5.2		
1.60	–11.8± 5.6		
2.00	–25.3± 6.4		
2.58	–17.1± 7.2		
3.56	–29.6± 5.7		
5.42	–25.3± 6.2		

Notes. Column 1: radius for the rotation speed profile. Column 2: rotation velocities. Column 3: radius for the velocity dispersion profile. Column 4: velocity dispersions. All the kinematic profiles are electronically available.

Figures 2–5 clearly show that data with S/N below 15 might induce errors as large as 22% in determining σ, in particular for small velocity dispersions ($\sigma \sim 20$ km s^{-1}), while only 0.4% for radial velocities.

All these tests have been computed for the different wavelength ranges covered by our survey and the results obtained are rather similar. For the red arm of ISIS, where the instrumental resolution is higher, we have similar results to those shown in the blue arm (Figs. 2–5) but with slightly larger uncertainties.

These simulations show that radial velocities can be computed with spectra of S/N as low as 10 given that the uncertainty is always below 1%. However, in the study of velocity dispersions, we must discard any measurement with S/N below 15 because σ is, in this case, highly dependent on age and not reliable for σ as low as half the instrumental resolution.

When running the MOVEL algorithm as a function of galaxy radius, we fitted the optimal template at every radius, rather than using the central optimal template, in order to improve the fit. As a result, the optimal templates turn out to be radially dependent. The differences, however, are not very large, because in the linear combination of templates, G-stars always contribute with the highest weight.

More than one kinematic profile per galaxy was obtained from the different instrumental configurations used in the observation campaigns (see Table 1). These profiles, consistent within the errors, were averaged to produce a single, high S/N profile per galaxy (see Fig. 6).

The recessional velocity of each single galaxy, removed for the determination of the rotation curve (Fig. 6), has been determined by averaging, with a weighted mean, the recessional velocity measured in each single position along the radius. This improved technique for measuring recessional velocities (listed in Table 4) can be applied since the rotation curves are symmetrical[3].

Table 3 gives an example of the tables electronically available with the values of the kinematic profiles.

---

[3] Galaxies such as VCC856, those with the poorest quality, have a nonzero central velocity.

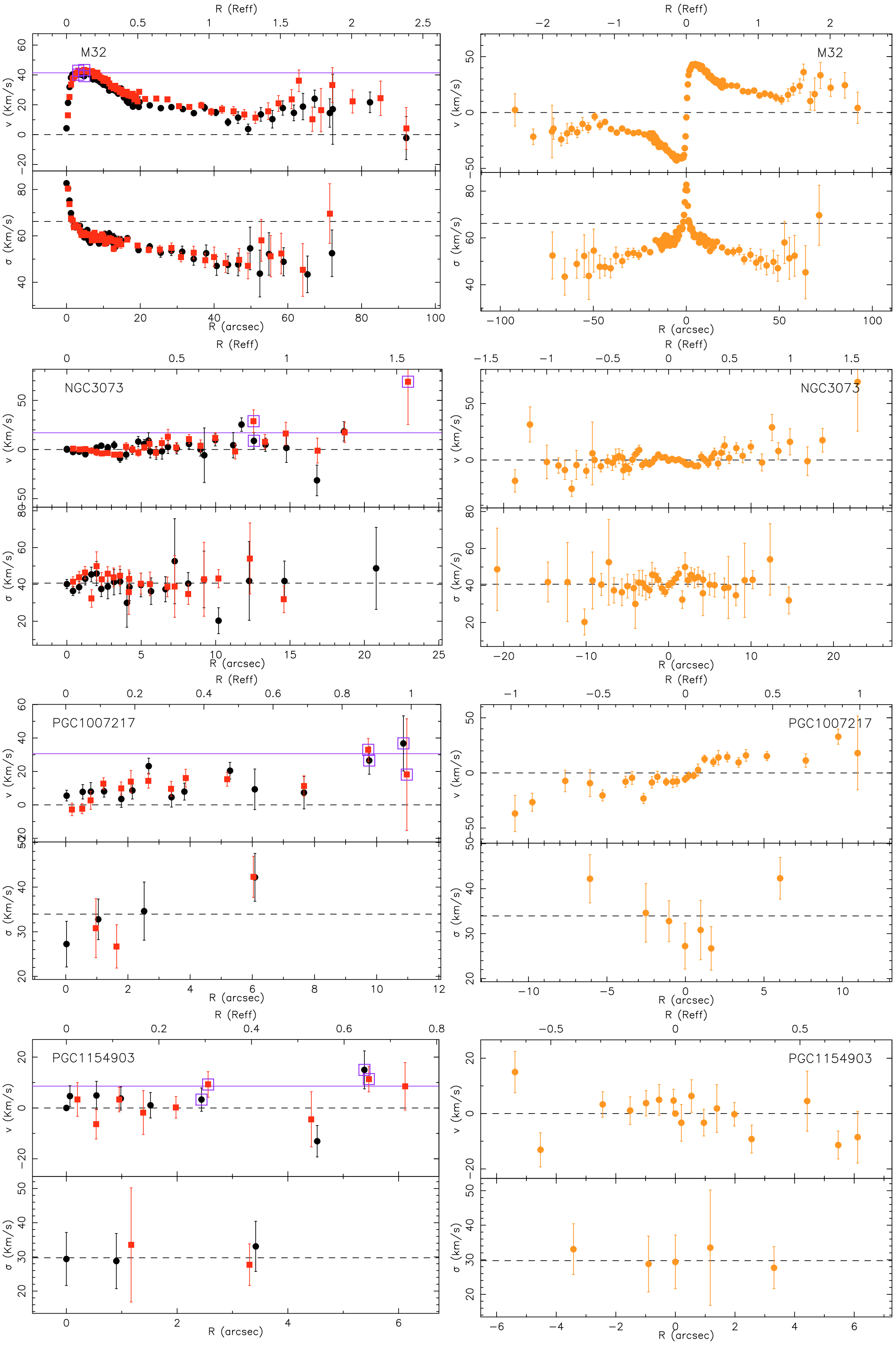

Fig. 6. Kinematic profiles of the galaxy sample. Each diagram shows the folded rotation curve of the galaxy in the *left upper panel* and in the *left bottom panel* the folded velocity dispersion profile. The different sides of the galaxy are indicated with red squares and black dots. The *upper* x-axis gives the radius as a fraction of the effective radius (R_{eff}) of each galaxy in the I band (see Sect. 6). The purple open squares show the points used to calculate the maximum rotation for each galaxy and the purple line indicates this $v_{\max}$. The dashed line in the velocity dispersion profiles indicates the central σ computed up to the R_{eff} (see Table 4). In the right panels the not-folded kinematical profiles are plotted.

Table 4. Kinematic parameters.

Galaxy	σ (km s^{-1})	$v_{\max}$ (km s^{-1})	$(v_{\max}/\sigma)^*$	$v_{\rm rad}$ (km s^{-1})
PGC1007217	35.2 ± 0.9	30.6 ± 5.0	2.3 ± 0.4	1592.3 ± 3.3
PGC1154903	23.1 ± 4.1	8.6 ± 2.6	0.5 ± 0.2	1156.3 ± 6.4
NGC 3073	39.8 ± 0.3	17.1 ± 6.7	1.1 ± 0.4	1168.9 ± 2.5
VCC21	26.1 ± 4.0	18.4 ± 5.9	0.9 ± 0.3	463.6 ± 9.2
VCC308	31.7 ± 1.2	30.4 ± 8.6	1.0 ± 0.3	1515.3 ± 3.2
VCC397	29.9 ± 1.1	52.0 ± 11.6	2.5 ± 0.6	2434.9 ± 2.4
VCC523	45.8 ± 0.7	39.6 ± 5.7	1.5 ± 0.2	1515.7 ± 2.6
VCC856	29.6 ± 2.5	9.7 ± 1.9	1.0 ± 0.2	980.2 ± 1.9
VCC917	31.4 ± 1.4	21.6 ± 7.5	0.8 ± 0.3	1236.2 ± 2.4
VCC990	40.6 ± 1.0	26.3 ± 1.6	0.9 ± 0.1	1691.5 ± 2.1
VCC1087	48.3 ± 0.7	7.1 ± 6.4	0.2 ± 0.2	644.6 ± 3.2
VCC1122	37.2 ± 0.8	17.3 ± 7.7	0.5 ± 0.2	447.8 ± 2.7
VCC1183	41.3 ± 1.2	10.1 ± 2.8	0.5 ± 0.1	1290.7 ± 2.3
VCC1261	51.8 ± 0.9	13.9 ± 5.2	0.4 ± 0.1	1806.4 ± 2.1
VCC1431	54.1 ± 1.2	7.0 ± 3.6	0.1 ± 0.1	1472.8 ± 3.1
VCC1549	38.9 ± 1.9	5.2 ± 2.2	0.3 ± 0.1	1377.3 ± 2.9
VCC1695	28.7 ± 1.1	14.3 ± 3.1	0.9 ± 0.2	1706.0 ± 3.0
VCC1861	40.4 ± 0.9	6.3 ± 4.3	0.2 ± 0.1	617.2 ± 2.6
VCC1910	39.0 ± 1.1	6.0 ± 2.3	0.4 ± 0.2	178.6 ± 2.2
VCC1912	37.1 ± 1.0	20.8 ± 4.5	0.5 ± 0.1	-110.5 ± 2.0
VCC1947	45.3 ± 1.1	28.3 ± 2.1	1.1 ± 0.1	956.3 ± 1.8

Notes. Column 2: central velocity dispersions computed within the $R_{\rm eff}$. Column 3: maximum rotation velocities. The $v_{\max}$ adopted for VCC0856, VCC0990, and VCC1183 have been measured in the rotation curves of Chilingarian (2009) due to their larger extent (see Sect. 5.3). Column 4: anisotropy parameter corrected from inclination. Column 5: mean radial velocity observed. These values agree with those of NED database.

5.2. Central velocity dispersion and maximum rotational velocity

To compute the central velocity dispersion (σ) we shifted all the spectra to the same wavelength scale using the rotation curves displayed in Fig. 6, and we coadded all the individual spectra up to one effective radius. The typical S/N for the spectrum where the central σ is computed is ~60 Å^{-1}. These results are shown in Table 4.

The maximum rotational velocity ($v_{\max}$) was calculated as the weighted average of the two highest velocities along the major axis on both sides of the galaxy at the same radius. For non-symmetric profiles, at least three values were required. As a consequence, values with larger errors weigh less than those with smaller errors. For each galaxy these values are presented in Fig. 6 as purple squares. We show in Appendix A that, given the uncertainty, all galaxies with $v_{\max} < 9$ km s^{-1} can be considered non-rotators.

The ratio between these two kinematic measurements, the maximum rotation velocity $v_{\max}$, and the velocity dispersion σ is called anisotropy parameter, $v_{\max}/\sigma$, and it is used to study the rotational/pressure support of the galaxies. In Table 4 we show $(v_{\max}/\sigma)^*$, the anisotropy parameter corrected for the inclination. This correction is done following the expression $(v_{\max}/\sigma)^* = \frac{v_{\max}/\sigma}{\sqrt{\epsilon/(1-\epsilon)}}$, where ϵ is the ellipticity. For those galaxies with ellipticity close to zero, no correction can be made because they are nearly face on. We choose a conservative value of $(v_{\max}/\sigma)^* = 0.8$ as the limit between pressure and rotationally supported systems in order to include those objects that, within the errors, are consistent with being flattened by rotation. This assumption is justified by the fact that the measured $v_{\max}$ is a lower limit since the rotation curves are still rising.

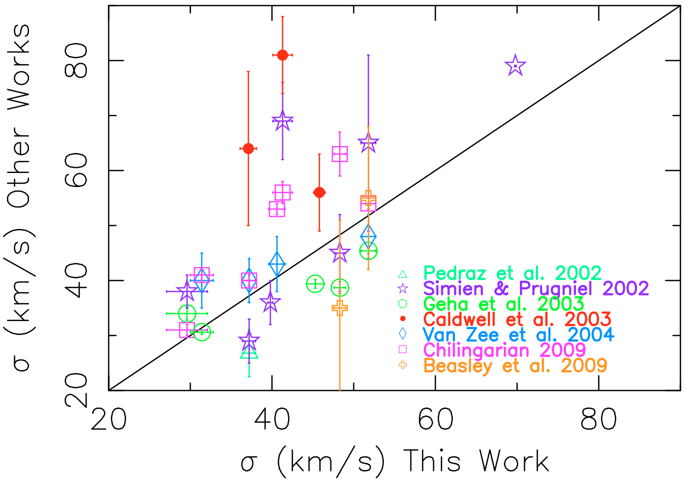

Fig. 8. Comparison between the velocity dispersions measured in this work and those of other authors. The colours and symbols are the same as in Fig. 7. We add a comparison with Caldwell et al. (2003) (solid red points), who only measured central values and no kinematical profiles.

5.3. Comparison to the literature

When displaying the kinematic profiles measured in this work simultaneously with those of other authors (Fig. 7), one sees that the radial extent of the kinematic curves varies from one work to another. In addition, the offsets found in the velocity dispersions are not always consistent within the errors (Fig. 8). These two differences are important, because different radial extents lead to different maximum rotation velocities, and offsets in the velocity dispersion profiles lead to different central σ values.

5.3.1. Velocity dispersions

There are two factors that critically affect the measurements of the velocity dispersion of the galaxies: the unidentical instrumental σ for the stars and the galaxies and the spectral types of the stars used to fit the width of the galaxy lines. Caldwell et al. (2003) made their observations with a $\sigma_{\rm inst} = 100$ km s^{-1}, which is too high to accurately measure velocity dispersions of typical dwarf galaxies, below 50 km s^{-1}.

Concerning the equality of the instrumental resolution in the templates and in the galaxies, Chilingarian (2009) used simple stellar population (SSP) models of PEGASE.HR (Le Borgne et al. 2004), based on the empirical stellar library ELODIE (Prugniel et al. 2007) ($R = 10\,000$). In this case, the broadening of the SSP models to $\sigma_{\rm inst}$ of the galaxies must be cautiously done because $\sigma_{\rm inst}$ of the models is the mean value of the spectral resolution of the library they are based on, therefore small differences after the broadening between the SSP models and the galaxies can arise.

Continuing with the same effect, in the works of Pedraz et al. (2002) and van Zee et al. (2004b) the stars observed were not filling the slit because they were not defocused and the seeing was smaller than their slit width. But in the case of Geha et al. (2003) and Beasley et al. (2009), where their slit widths were 0.75″ and 1.0″ respectively, it is possible that some stars were filling the slit thanks to the seeing. However, in none of these works was a correction made to assure that the instrumental profile in the stars was the same as in the galaxies.

In reference to the templates used to perform σ, some of the authors mentioned above used only one star to fit the galaxy spectrum, and in such a case the fact that the template is not

Table 5. Uncertainties introduced when different templates are used to calculate the velocity dispersion of a dwarf galaxy with different stellar populations.

	$\frac{\Delta\sigma}{\sigma} \times 100$		
Age (Gyr)	$Z = +0.0$	$Z = -0.4$	$Z = -0.7$
Linear combination of B to M stars			
1	15%	19%	1%
4	8%	18%	19%
10	7%	14%	23%
G8III			
1	32%	54%	71%
4	15%	18%	20%
10	17%	13%	11%
K1III			
1	29%	47%	59%
4	19%	18%	20%
10	17%	13%	11%

Notes. $\Delta\sigma/\sigma$, defined in Fig. 2, uses as $\sigma_{\rm i}$ 40 km s^{-1}.

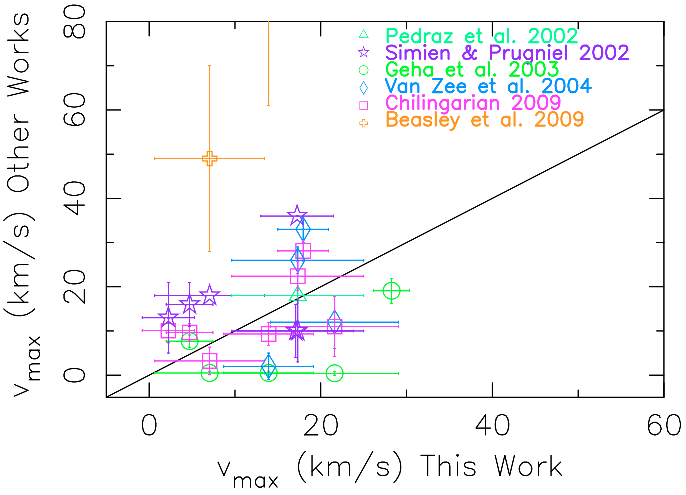

Fig. 9. Comparison between the maximum rotational velocity measured in this work and those measured by other authors. Symbols and colours are the same as in Fig. 7. VCC1261 from Beasley et al. (2009) is nearly outside the plot due to its enormous rotation: 105 ± 44 km s^{-1}.

representative of the stellar population of the galaxy might lead to large errors. We computed Monte-Carlo simulations to see the differences between fitting the galaxy spectrum with only one star and a linear combination of stars of spectral types from B to M, with different luminosity classes. The simulations consisted of a selection of PEGASE.HR models of 3 different ages (1 Gyr, 4 Gyr and 10 Gyr) and 3 different metallicities ($Z = 0.0$, $Z = -0.4$, $Z = -0.7$) with Salpeter IMF (Le Borgne et al. 2004): a total of 9 models. The stars used as templates were from the MILES library (Sánchez-Blázquez et al. 2006). First of all we checked that, after broadening the models (originally at $FWHM = 0.55$ Å) to the MILES resolution ($FWHM = 2.3$ Å), we obtained $\sigma = 0$ km s^{-1} when running MOVEL, thereby showing that there was no zero point offset. Secondly, we broadened the models to 40 km s^{-1} to simulate dwarf galaxies of different stellar populations. And finally, we ran MOVEL using 3 different kinds of templates: only one K1III star, as in Geha et al. (2003), only one G8III star, as in van Zee et al. (2004b), and a linear combination of B to M stars with different luminosity classes, as in this work. To measure σ we masked the Balmer lines, especially those bluer than H$_\delta$ to avoid possible problems from emission lines. Our simulations show that a linear combination of different stars is the most accurate method of obtaining the velocity dispersion of the galaxies, never finding an error above 25%, independent of the stellar population considered. If a young population dominates the light of the galaxy (for ages of 1 Gyr and below), and a single G or K star is used as a template, an error up to 70% can be achieved. When a single star is used as template, a dependence on metallicity for young populations (1 or 4 Gyr) is also found, in the sense that decreasing the metallicity increases the uncertainty. This dependence is very likely due to offsets introduced by the method employed to compute σ. The results obtained have been summarised in Table 5.

5.3.2. Rotation curves

Different criteria have been used in the literature to measure the maximum rotation velocity. The main difficulty here is to have an extended rotation curve that reaches a clear plateau where the maximum rotation can be measured. As this is not so easy for dEs, an objective criterion that is independent of the shape of the rotation curve in each case must be adopted. The different criteria used by the various authors have led to maximum rotational velocities that are nevertheless nearly consistent within the errors in the majority of the cases (Fig. 9). The criterion used by Pedraz et al. (2002) is the same as the one adopted here. Although we achieved a radial extent of 23″ for VCC1122 and Pedraz et al. (2002) only 8″, the latter value was enough to reach the flat part of the rotation curve, and, as a consequence, both measurements of the maximum rotation are identical. The explanation for the differences found with Simien & Prugniel (2002) are mainly based on the fact that only two points were considered to obtain the maximum rotation in that paper. The differences with Geha et al. (2003) stem from the limitation of their data to the core of the galaxies, never reaching radii larger than 6″ (see Fig. 7). The differences with van Zee et al. (2004b) and Chilingarian (2009) are related to the different radial extents of the rotation curves. Chilingarian (2009) does not calculate the maximum rotation, but we applied our criterion to his rotation curves. Finally, the differences found with Beasley et al. (2009) are because $v_{\rm max}$ is obtained from the analysis of globular clusters located up to ~7$R_{\rm eff}$. When their kinematics, determined from the stellar component using long-slit spectroscopy along the major axis of the galaxy, are compared to our data, the agreement is evident (Fig. 7). The maximum rotation values adopted for the analysis (see Table 4) are our own values, except for VCC856, VCC990, and VCC1183, where the data come from Chilingarian (2009) since he obtained larger radii than ours. The values from Beasley et al. (2009) cannot be adopted here because our work is dedicated to analysis of the stellar component of dEs.

The comparison with Beasley et al. (2009), who finds much higher rotation speeds at 7$R_{\rm eff}$ (100 and 50 km s^{-1} higher for VCC1087 and VCC1261, respectively) than our data at $R_{\rm eff}$, indicate that the rotation curves of these galaxies are still rising.

6. Photometric parameters

Comparison with some photometric parameters is needed for a complete analysis of the kinematics. For our study, we require I-band (Johnson-Cousins) total magnitudes and optical radii ($R_{\rm opt}$, radius containing 83% of the total I-band luminosity, Catinella et al. 2006) to study the shape of the rotation curves. Effective radii ($R_{\rm eff}$, radius containing 50% of the total light) are needed to measure the extent of the radial profiles in physical units of

Table 6. Derived parameters.

Galaxy	d (Mpc)	M_I (mag)	ϵ	$R_{\rm eff}$ ($''$)	$C_4 \times 100$	Disk classification (L06b)
PGC1007217	20.23 ± 1.40	−17.39 ± 0.15	0.13 ± 0.05	11.11 ± 0.02	$4.8^{(*)} \pm 0.6$	–
PGC1154903	15.00 ± 1.10	−15.91 ± 0.16	0.34 ± 0.02	8.36 ± 0.04	0.3 ± 4.4	—
NGC 3073	33.73 ± 14.44	−20.43 ± 0.93	0.14 ± 0.02	14.78 ± 0.03	$3.2^{(*)} \pm 0.2$	–
VCC21	16.74 ± 0.15	−17.78 ± 0.03	0.36 ± 0.03	15.48 ± 0.11	$3.7^{(*)} \pm 0.6$	Disk
VCC308	16.41 ± 0.32	−18.78 ± 0.05	0.04 ± 0.03	19.22 ± 0.04	0.2 ± 2.0	Disk
VCC397	16.41 ± 0.32	−17.62 ± 0.05	0.33 ± 0.03	13.75 ± 0.02	$5.1^{(*)} \pm 0.3$	Disk
VCC523	16.74 ± 0.15	−19.16 ± 0.03	0.25 ± 0.01	20.90 ± 0.03	$2.6^{(*)} \pm 0.3$	Disk
VCC856	16.83 ± 0.46	−18.49 ± 0.06	0.09 ± 0.03	15.82 ± 0.06	–0.2 ± 1.7	Disk
VCC917	16.74 ± 0.15	−17.39 ± 0.03	0.41 ± 0.02	9.68 ± 0.04	$4.3^{(*)} \pm 0.2$	No Disk
VCC990	16.74 ± 0.15	−18.27 ± 0.03	0.34 ± 0.02	9.73 ± 0.02	$4.1^{(*)} \pm 0.3$	Disk
VCC1087	16.67 ± 0.46	−18.94 ± 0.06	0.28 ± 0.03	22.74 ± 0.05	–0.9 ± 1.1	No Disk
VCC1122	16.74 ± 0.15	−17.94 ± 0.03	0.50 ± 0.04	14.06 ± 0.05	$3.8^{(*)} \pm 0.2$	No Disk
VCC1183	16.74 ± 0.15	−18.59 ± 0.03	0.22 ± 0.12	18.23 ± 0.01	$1.7^{(*)} \pm 0.0$	Disk
VCC1261	18.11 ± 0.50	−19.39 ± 0.06	0.37 ± 0.05	22.07 ± 0.03	$1.5^{(*)} \pm 0.6$	No Disk
VCC1431	16.14 ± 0.45	−18.47 ± 0.06	0.03 ± 0.01	10.32 ± 0.01	0.2 ± 0.1	No Disk
VCC1549	16.74 ± 0.15	−18.18 ± 0.03	0.16 ± 0.01	13.56 ± 0.05	–1.3 ± 3.5	No Disk
VCC1695	16.52 ± 0.61	−18.13 ± 0.08	0.22 ± 0.05	19.78 ± 0.10	–0.9 ± 3.7	Disk
VCC1861	16.14 ± 0.45	−18.57 ± 0.06	0.04 ± 0.02	18.52 ± 0.04	0.8 ± 2.5	No Disk
VCC1910	16.07 ± 0.44	−18.63 ± 0.06	0.14 ± 0.04	13.70 ± 0.02	–0.4 ± 1.0	Disk
VCC1912	16.74 ± 0.15	−18.62 ± 0.03	0.54 ± 0.06	23.34 ± 0.02	$3.6^{(*)} \pm 0.2$	No Disk
VCC1947	16.74 ± 0.15	−18.46 ± 0.03	0.23 ± 0.01	10.70 ± 0.02	$4.2^{(*)} \pm 0.5$	–

Notes. Column 2: distances in Mpc from surface brightness fluctuations (SBF) for individual Virgo galaxies from Mei et al. (2007) when available, or the mean A/B cluster distance from Mei et al. (2007) for the rest of them (note that E, N and S clouds are east, north and south areas of cluster A). The distance for NGC 3073 from SBF by Tonry et al. (2001) and PGC1007217 and PGC1154903 distances are from NED/IPAC database derived from redshift with $H_0 = 73 \pm 5$ km s^{-1} Mpc^{-1} (use cautiously). Column 3: Absolute magnitudes in I-band (Johnson-Cousins in AB system) converted from i-band measured in SDSS images using $m_I = m_i - 0.52$ mag. Column 4: ellipticities from i-band (SDSS) images. The quoted errors indicate the rms scatter in the ellipticity between $3''$ and the $R_{\rm eff}$. Column 5: Effective radius from i-band (SDSS) images. Column 6: diskyness/boxyness parameter from i-band (SDSS) images. The asterisks indicate C_4 measured as the maximum in the region $3''$–$3R_{\rm eff}$ if prominent disky features are found; in the rest of the cases the quoted values are the average in this same radial range and the errors the RMS scatter (see Appendix D). Column 7: Lisker et al. (2006b) classification, where a dash indicates that these galaxies are not included in their analysis.

the galaxy. Ellipticities (ϵ) are needed to make the appropriate corrections for inclination. A parameter to measure the boxyness/diskyness of the isophotes (C_4) is also required to study the possibly late-type origin of these dwarf early-type galaxies.

All these parameters were obtained from i-band Sloan Digital Sky Survey (SDSS, York et al. 2000) data release 6 (DR6, Adelman-McCarthy et al. 2008) photometry. They were calculated using the IRAF[4] task ELLIPSE as described in Appendix B. The transformation from i-band (SDSS) to I-band (Johnson-Cousins) was done assuming $m_I = m_i - 0.52 \pm 0.01$ mag (Fukugita et al. 1995).

6.1. C_4: boxyness/diskyness parameter

The boxyness/diskyness (C_4) parameter measures the deviations of the isophotes from a perfect ellipse. If $C_4 > 0$, the isophotes are disky, indicating that some disk substructure is present in the galaxy, and the isophotes are boxy when $C_4 \leq 0$ (Carter 1978; Kormendy & Bender 1996). This parameter is independent of the surface brightness profile of the galaxy. The C$_4$ parameter, determined for our galaxies as described in Appendix D, is provided in Table 6.

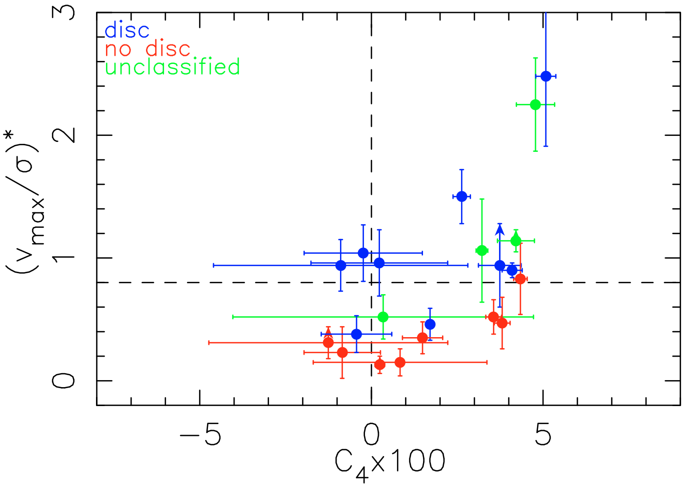

Fig. 10. Correlation between the anisotropic parameter $(v_{\rm max}/\sigma)^*$ and C_4x100. Colours indicate the Lisker et al. (2006b) classification. The galaxies with $v_{\rm max}$ measured inside the central $6''$ are considered lower limits and are indicated with arrows. The horizontal dashed line at $(v_{\rm max}/\sigma)^* = 0.8$ indicates a rough boundary between pressure and rotationally supported galaxies. The blue points are classified as having a disk in Lisker et al. (2006b), whereas no disk is found for the red points in that paper. See Appendix D for a discussion.

Our C_4 classification for disky isophotes agrees in general with the morphological classification of Lisker et al. (2006a) as can be seen in Fig. 10. Lisker et al. (2006a) classified a galaxy as disky when disk features (spiral arms, edge-on disks, or bars) were detected after subtracting an axisymmetric light distribution from the original image or after unsharp masking. In this

---

[4] IRAF is distributed by the National Optical Astronomy Observatory, which is operated by the Association of Universities for Research in Astronomy, Inc., under cooperative agreement with the National Science Foundation.

figure we can see that those galaxies classified as being without underlying structures in Lisker et al. (2006a), are grouped around $C_4 \leq 0$ (boxy or elliptical isophotes), while the galaxies with some disky structure in Lisker et al. (2006a) are all consistent with $C_4 > 0$ (disky isophotes). This justifies the use of the C_4 parameter to detect an underlying disk. Three exceptions are found and discussed in Appendix D.

In this respect, it is important to underline the correlation between C_4 and the anisotropic parameter evident in Fig. 10, first found by Bender et al. (1988) for more massive elliptical galaxies.

7. Analysis

The analysis presented in this work is primarily focused on the rotationally supported systems. Although the majority of the dwarf galaxies (15 out of 21) show some rotation ($v_{\max} > 9$ km s^{-1}, Table 4), only 11 are rotationally supported ($(v_{\max}/\sigma)^* > 0.8$) (Toloba et al. 2009). Here we try to understand whether the observed kinematic properties of the rotationally supported systems are consistent with those of star-forming galaxies of similar luminosity.

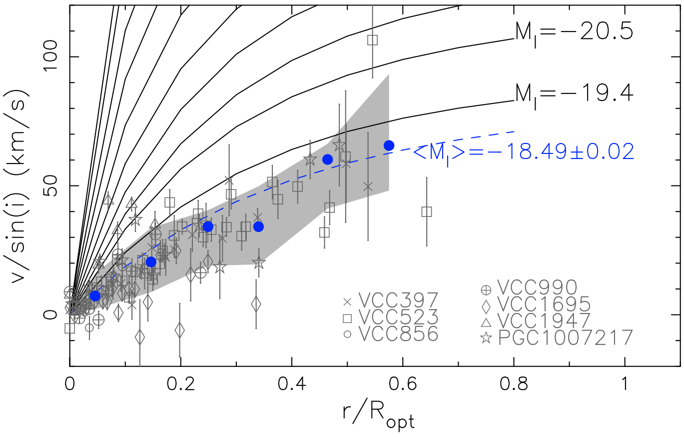

Fig. 11. The observed rotation curves of rotationally supported dEs (grey symbols) compared to the mean rotation curves of late-type spiral galaxies (black solid and blue dashed lines) from Catinella et al. (2006). Blue filled dots represent the median observed rotation curve of rotationally supported dE in bins of $r/R_{\rm opt} = 0.1$. The last bin contains all data for $r/R_{\rm opt} \geq 0.5$. The grey area indicates rotation velocities within 1σ from the median.

7.1. Shape of the rotation curves

Catinella et al. (2006) made a systematic study of the shape of the rotation curves of late-type spiral galaxies as a function of luminosity based on the method described in Persic et al. (1996). They fitted the rotation curves following the Polyex model (Giovanelli & Haynes 2002), which has the form

$$V_{\rm PE}(r) = V_0\left(1 - e^{-r/r_{\rm PE}}\right)\left(1 + \frac{\alpha r}{r_{\rm PE}}\right). \tag{1}$$

This analytical function depends on 3 parameters V_0, $r_{\rm PE}$, and α, which represent the amplitude, the exponential scale of the inner region, and the slope of the outer part of the rotation curve. The mean fitted rotation curves from Catinella et al. (2006) are normalised to the optical radius ($R_{\rm opt}$, radius containing 83% of the total I-band luminosity), and the velocities are corrected from inclination. To compare them with our rotationally supported galaxies, we calculated the inclinations as in Giovanelli et al. (1997a):

$$\cos^2 i = \frac{(1-\epsilon)^2 - q_0^2}{1 - q_0^2} \tag{2}$$

where i is the inclination, ϵ is the ellipticity, and q_0 is a constant value that depends on the thickness of the disk. Here we assume $q_0 = 0.3$, a conservative value for dwarf galaxies shaped as thick disks (Lisker et al. 2007)[5].

The comparison between the mean rotation curves of Catinella et al. (2006) and those of our rotationally supported objects must be done in the same luminosity regime since the derived parameters of the Polyex model are luminosity dependent. As the dwarf galaxies analysed in this work have magnitudes below the minimum magnitude in Catinella et al. (2006) ($M_I = -19.4$), the reference Polyex model of low-luminosity star-forming systems has been determined by extrapolating linearly the three faintest values of the Polyex parameters to $M_I = -18.49$, the mean I-band magnitude of the galaxies here analysed. The parameters used to construct this curve are $V_0 = 74.58$ km s^{-1}, $r_{\rm PE} = 0.35''$ and $\alpha = 0.03$.

In Fig. 11 we compare the mean fitted rotation curves of Catinella et al. (2006) for late-type spirals (obtained from emission lines) with the rotation curves of our rotationally supported dEs determined from absorption lines. Of the 11 rotationally supported dEs, only 7 have been considered for this analysis because 3 of them, VCC21, VCC917, and NGC 3073, have poor quality rotation curves ($\frac{\Delta v_{\max}}{v_{\max}}$ over 25%), and VCC308 has ϵ lower than 0.1, implying that the galaxy is nearly face on. Figure 11 shows the median rotation curve of our dEs in bins of $\frac{r}{R_{\rm opt}} = 0.1$ and its 1σ deviation (containing 68% of the values). Polyex model was extrapolated to $M_I = -18.49$.

It is evident from Fig. 11 that our rotationally supported galaxies are characterised by rotation curves that are similar to those of late-type spiral galaxies of equal luminosity; in other words, galaxies with similar rotation curves have similar absolute magnitudes despite their morphological type. We see that rotationally supported dEs dynamically behave like small late-type spiral galaxies.

It is interesting to see that, despite their similar exponential radial light distribution, dEs have two different kinematic behaviours and can be either pressure or rotationally supported. Furthermore, rotationally supported dEs have rotation curves similar to those late-type spirals even though these latter objects are gas-dominated systems.

7.2. Tully-Fisher relation

Given the similarity in the kinematic properties of rotation-supported dEs with those of late-type spirals, we expect that these systems follow the Tully-Fisher relation, as first proposed by van Zee et al. (2004b). The Tully-Fisher relation is a typical scaling relation valid for star-forming, rotating systems, linking the total luminosity to the maximal rotation velocity of the galaxy.

---

[5] For early-type spirals $q_0 = 0.2$ (Giovanelli et al. 1997a). The most recent measurements of the thickness of dwarf galaxies gives $q_0 = 0.3{-}0.35$ (Sánchez-Janssen et al. 2010). The difference in $v_{\max}$ after the correction for inclination between using $q_0 = 0.2$ and $q_0 = 0.35$ is of 4.4%, insignificant.

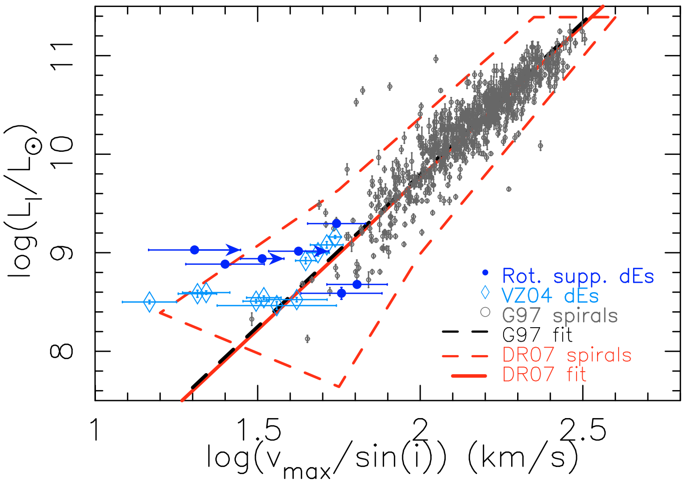

Fig. 12. Tully-Fisher relation for 7 of our rotationally supported dEs (in dark blue), the dEs from van Zee et al. (2004a,b, VZ04, in light blue), the normal spirals from Giovanelli et al. (1997b, G97, in grey) and De Rijcke et al. (2007, DR07, red limited area). Absolute magnitudes of dEs have been obtained using distances from Mei et al. (2007) (criterion described in Table 6). For Giovanelli et al. data we use H_0 = 73 km s^{-1} Mpc^{-1} (Mei et al. 2007). The arrows indicate lower limits of $v_{\rm max}$ (those obtained in the inner 6″). Fits of the Tully-Fisher relation are indicated in black for the normal spirals of Giovanelli et al. (1997b) and in red for De Rijcke et al. (2007, DR07). DR07 fit has been transformed to I band using the colour-morphology relation from Fukugita et al. (1995) and using H_0 = 73 km s^{-1} Mpc^{-1} and $M_{I\odot} = 4.08$ and $M_{B\odot} = 5.48$ from Binney & Merrifield (1998).

Table 7. Dynamical and stellar mass-to-light ratios in I-band in solar units.

Galaxy	$(\Upsilon_I)_\odot$	$(\Upsilon_I^*)_\odot$
PGC1007217	4.0 ± 0.8	1.9
PGC1154903	1.8 ± 3.1	1.2
NGC 3073	0.6 ± 0.4	0.2
VCC21	1.5 ± 0.4	0.5
VCC308	1.5 ± 0.3	1.1
VCC397	4.8 ± 1.2	0.9
VCC523	2.2 ± 0.2	1.3
VCC856	1.1 ± 0.2	2.0
VCC917	2.5 ± 0.4	2.4
VCC990	1.9 ± 0.1	2.8
VCC1087	2.3 ± 0.1	2.4
VCC1122	2.4 ± 0.1	2.2
VCC1183	1.9 ± 0.1	1.4
VCC1261	2.3 ± 0.1	1.4
VCC1431	2.3 ± 0.1	3.4
VCC1549	2.1 ± 0.2	3.1
VCC1695	1.7 ± 0.3	1.2
VCC1861	1.6 ± 0.1	2.8
VCC1910	1.6 ± 0.1	3.2
VCC1912	2.1 ± 0.1	0.6
VCC1947	1.8 ± 0.1	1.7

Notes. $(\Upsilon_I^*)_\odot$ is only indicative, the large errors in the stellar populations (Michielsen et al. 2008) make the uncertainties of $(\Upsilon_I^*)_\odot$ of the same order of magnitude as the values.

In Fig. 12 we compare the Tully-Fisher relation for ours[6] and the van Zee et al. (2004b) dEs to that of the normal late-type galaxies of Giovanelli et al. (1997b) and De Rijcke et al. (2007). Figure 12 clearly shows that these rotationally supported dEs follow the Tully-Fisher relation with a similar scatter to the normal spirals of De Rijcke et al. (2007) and thus kinematically behave as late-type spirals. The $v_{\rm max}$ of dEs plotted in Fig. 12 is probably a lower limit since it is generally measured where the rotation curve is still rising, as suggested by the kinematics of the globular clusters. It is thus conceivable that the agreement between the Tully-Fisher relation of rotationally supported dEs and late-type spirals of similar luminosity is even better than the one depicted in Fig. 12.

7.3. Dark matter content

The shape of the rotation curves gives information about the dark matter content and distribution of late-type galaxies (e.g., Catinella et al. 2006). Similarly, σ can be used to measure the dark matter content of pressure-supported systems. Following Beasley et al. (2009), we estimate the total dynamical mass of our sample galaxies using the relation

$$M_{\rm tot} = M_{\rm press} + M_{\rm rot} \tag{3}$$

where $M_{\rm press}$ is the mass inferred from the velocity dispersion after the contribution from rotation has been removed and $M_{\rm rot}$ is the mass deduced by the intrinsic rotation velocity of the galaxies. $M_{\rm press}$ inside the half-light radius is defined as in Cappellari et al. (2006):

$$\begin{aligned} M_{\rm press} &\simeq 2.5 G^{-1} \sigma^2 R_{\rm eff} \\ &\simeq 580 \left(\frac{\sigma^2}{\rm km^2\,s^{-2}}\right)\left(\frac{R_{\rm eff}}{\rm pc}\right) M_\odot. \end{aligned} \tag{4}$$

The rotation curves of rotationally supported systems are characterised by an approximately constant gradient, suggesting solid body rotation up to the $R_{\rm eff}$. In this case $M_{\rm rot}$ is given by the relation

$$\begin{aligned} M_{\rm rot} &= \frac{R_{\rm eff} v_{\rm max}^2}{G} \\ &= \left(\frac{R_{\rm eff}}{\rm pc}\right)\left(\frac{v_{\rm max}^2}{\rm km^2\,s^{-2}}\right)\left(\frac{1}{4.3\times 10^{-3}}\right) M_\odot. \end{aligned} \tag{5}$$

Dynamical mass-to-light ratios (Υ_I, Table 7) are then measured using the I-band luminosities and Eq. (4) for pressure supported systems and the sum of Eqs. (4) and (5) for rotationally supported objects[7]. Stellar mass-to-light ratios (Υ_I^*, Table 7) are computed using the models of single stellar populations (SSP) of Vazdekis et al. (2010) and the ages and metallicities from Michielsen et al. (2008).

Figure 13 presents the relation between the dynamical mass-to-light ratio and the absolute I-band magnitude for our galaxies (red and blue dots), the sample of classical elliptical galaxies from Cappellari et al. (2006, $\Upsilon_{\rm Jeans}$ in I-band), the dEs from Geha et al. (2002) and the Milky Way dwarf spheroidals (dSphs) from Wolf et al. (2010)[8]. NGC 3073 in not a dE given its high luminosity ($M_I = -20.4$ mag).

---

[6] No asymmetric drift is applied to either our dEs or to those of van Zee et al. (2004b). This correction would increase $v_{\rm max}$ by 2.5 ± 0.9 in those rotationally supported systems plotted in Fig. 12.

[7] This method of obtaining $M_{\rm tot}$ is equivalent to introducing the asymmetric drift.

[8] The Υ_I values of Wolf et al. (2010) have been converted to Eq. (4) for consistency.

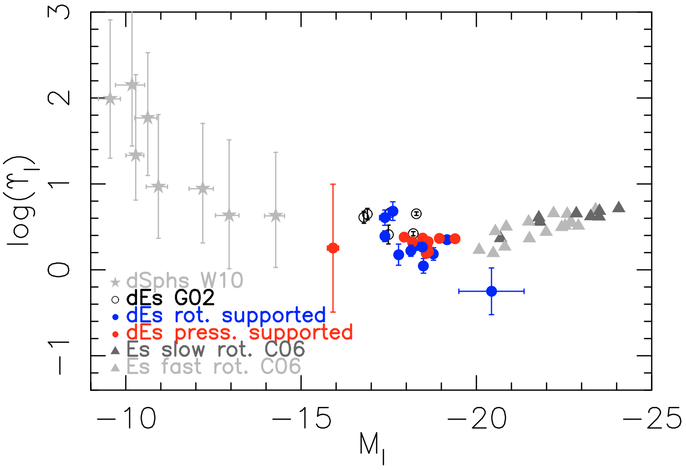

Fig. 13. Dynamical mass-to-light ratio as a function of the absolute magnitude in I-band. Red and blue dots indicate our pressure and rotationally supported dEs respectively. For comparison, open circles show dEs by Geha et al. (2002, G02), grey asterisks are dSphs from Wolf et al. (2010, W10), and dark and light grey triangles are slow and fast rotators from Cappellari et al. (2006, C06). The transformation to I band was performed using the colour-morphology relation by Fukugita et al. (1995) for Es. For the dwarf galaxies we used $V - I = 1.03 \pm 0.04$ as calculated by van Zee et al. (2004a).

In line with Zaritsky et al. (2006) and Wolf et al. (2010), we observe that the total mass-to-light ratio within the $R_{\rm eff}$ of dEs is the lower limit of the decreasing and increasing Υ_I vs. luminosity relations observed in giant ellipticals (Cappellari et al. 2006) and dSphs (Wolf et al. 2010), respectively. Dwarf early-type galaxies have on average $\Upsilon_I = 2.00 \pm 0.04\ \Upsilon_{I\odot}$, with a slightly higher dispersion in rotating systems (rms = $0.06\ \Upsilon_{I\odot}$) than in pressure-supported systems (rms = $0.04\ \Upsilon_{I\odot}$) .

Our sample of dEs have on average $M_{\rm dyn}/M^* = 1.6 \pm 1.2$ (obtained as the ratio between the dynamical and stellar mass-to-light ratios, Υ_I and Υ_I^*, respectively, Table 7), thus they are not dominated by dark matter within the $R_{\rm eff}$ (as previously suggested by Geha et al. 2002; Forbes et al. 2008), consistently with what is found is massive ellipticals (Cappellari et al. 2006) but contrary to dSphs (Wolf et al. 2010).

8. Discussion

How does this observational evidence compare with the different scenarios of galaxy formation? In a more general context we recall that, in the most recent hierarchical models of galaxy formation, only the most massive ellipticals have been formed through major merging events (De Lucia et al. 2006). The strong morphological segregation observed in high-density environments (Sandage et al. 1985; Ferguson & Binggeli 1994; Blanton et al. 2005) indicates that the cluster environment plays a major role in the formation of dEs.

In Toloba et al. (2009) we have shown that rotationally supported dEs, characterised by a disky structure, are primarily located in the field and in the periphery of the cluster, while pressure-supported systems are closer to the centre. We also found that rotationally supported dEs have, on average, younger stellar populations than pressure-supported systems. This evidence suggests that rotationally supported dEs are low-luminosity, late-type galaxies, which have recently entered the cluster and lost their gas because of the interaction with the hostile environment, having been transformed, on short time scales, into dEs. It thus seems clear that not all dwarf early-type galaxies are the low-luminosity extension of massive ellipticals.

The new kinematic data presented in this work support this scenario: rotationally supported systems have rotation curves similar to those of late-type galaxies of similar luminosity and follow the Tully-Fisher relation, the most representative scaling relation for late-type systems. Since the angular momentum of these objects is conserved, the most plausible scenario for gas stripping is the ram pressure exerted by the dense and hot IGM on the fragile ISM of the low-luminosity star forming galaxies freshly entering the cluster environment (see Boselli et al. 2008a,b, for an extensive discussion).

For these rotationally supported objects, gravitational interaction with the cluster potential or with other cluster members (galaxy harassment) can be excluded since they would, on relatively short time scales, reduce the angular momentum of the perturbed galaxies, leading to the formation of pressure-supported systems. This process, however, could still be invoked to explain the kinematic and structural properties of the remaining pressure-supported dEs populating the core of the cluster (half of our sample), whose statistical analysis of their scaling relations (fundamental plane) will be the subject of a future communication.

It is indeed possible that, as for the massive galaxies, gravitational interactions played a major role at early epochs, when the velocity dispersion of the cluster was lower than at the present epoch since galaxies were accreted through small groups (preprocesing) (Boselli & Gavazzi 2006).

9. Conclusions

We present medium resolution ($R \sim 3800$) spectroscopy for 21 dwarf early-type galaxies, 18 located in the Virgo cluster and three in the field. These spectra were obtained with the IDS at the INT(2.5 m) and with ISIS at the WHT(4.2 m) at El Roque de los Muchachos Observatory (La Palma, Spain). We used these data to measure the kinematic profiles of these systems and calculate their maximum rotation velocity, as well as their central velocity dispersion. To guarantee the reliability of the data, we compared our observations with the data of 972 simulated galaxies in five different wavelength ranges corresponding to those used during the observations, and we ran 100 Monte-Carlo simulations for each simulated galaxy. The comparison between observed data and simulations shows that the adopted data extraction technique is appropriate for measuring the kinematic parameters of the target galaxies. We have also shown that velocity dispersions cannot be measured for S/N below 15, while accurate results are obtained for radial velocities with $S/N \geq 10$.

Our analysis has shown that dEs have on average dynamical M/L within the effective radius smaller than those of massive ellipticals and dSphs (in average $\log(\Upsilon_I) = 0.3 \pm 0.0 \log(\Upsilon_{I\odot})$). We thus confirm that, within the effective radius, dEs are not dark matter dominated objects.

We found that rotationally supported dEs have rotation curves similar to those of star-forming systems with similar luminosity and follow the same Tully-Fisher relation. Combined with the evidence that these systems are young objects with disk-like structures generally located on the outskirts of the cluster (Toloba et al. 2009), these observations are consistent with a picture where these rotationally supported dEs result from the transformation of star-forming systems that recently entered the cluster and lost their gas through their interaction with the environment. The observed conservation of the angular momentum in the rotationally supported dEs suggests that a milder ram-pressure stripping event must be the one responsible for the gas removal preferentially to more violent gravitational interactions (harassment) which would rapidly heat up the perturbed systems. Therefore, all this evidence suggests that dEs are not the low luminosity extension of massive early-types, because if that was the case, all dEs would be rotating with $v_{\max}/\sigma$ higher than those of Es. However, a population of non-rotators has also been found and, in addition, the evidence that they are stripped late-type spirals is strong enough to consider it as a possible origin of dEs in clusters.

Acknowledgements. We thank the MAGPOP EU Marie Curie Training Network for financial support for the collaborating research visits and observations that led to this paper. E.T. acknowledges the financial support by the Spanish research project AYA2007-67752-C03-03. We thank Consolider-GTC project for partial financial support. This paper made use of the following public databases: SDSS, NED, HyperLEDA, GOLDMine. We are grateful to the anonymous referee for a critical report that has improved the quality of the paper.

References

Adelman-McCarthy, J. K., Agüeros, M. A., Allam, S. S., et al. 2008, ApJS, 175, 297
Beasley, M. A., Cenarro, A. J., Strader, J., & Brodie, J. P. 2009, AJ, 137, 5146
Bender, R., Doebereiner, S., & Moellenhoff, C. 1988, A&AS, 74, 385
Bender, R., Burstein, D., & Faber, S. M. 1992, ApJ, 399, 462
Binggeli, B., Sandage, A., & Tammann, G. A. 1985, AJ, 90, 1681
Binney, J., & Merrifield, M. 1998, Galactic astronomy (Princeton Series in Astrophysics)
Blanton, M. R., Lupton, R. H., Schlegel, D. J., et al. 2005, ApJ, 631, 208
Boselli, A., & Gavazzi, G. 2006, PASP, 118, 517
Boselli, A., Cortese, L., Deharveng, J. M., et al. 2005, ApJ, 629, L29
Boselli, A., Boissier, S., Cortese, L., & Gavazzi, G. 2008a, ApJ, 674, 742
Boselli, A., Boissier, S., Cortese, L., & Gavazzi, G. 2008b, A&A, 489, 1015
Byrd, G., & Valtonen, M. 1990, ApJ, 350, 89
Caldwell, N., Rose, J. A., & Concannon, K. D. 2003, AJ, 125, 2891
Cappellari, M., Bacon, R., Bureau, M., et al. 2006, MNRAS, 366, 1126
Cardiel, N. 1999, PhD Thesis, Universidad Complutense de Madrid, Spain
Carter, D. 1978, MNRAS, 182, 797
Catinella, B., Giovanelli, R., & Haynes, M. P. 2006, ApJ, 640, 751
Cenarro, A. J., Cardiel, N., Gorgas, J., et al. 2001, MNRAS, 326, 959
Chilingarian, I. V. 2009, MNRAS, 394, 1229
De Lucia, G., Springel, V., White, S. D. M., Croton, D., & Kauffmann, G. 2006, MNRAS, 366, 499
De Rijcke, S., Zeilinger, W. W., Hau, G. K. T., Prugniel, P., & Dejonghe, H. 2007, ApJ, 659, 1172
Ferguson, H. C., & Binggeli, B. 1994, A&ARv, 6, 67
Ferrarese, L., Côté, P., Jordán, A., et al. 2006, ApJS, 164, 334
Fitzpatrick, E. L. 1999, PASP, 111, 63
Forbes, D. A., Lasky, P., Graham, A. W., & Spitler, L. 2008, MNRAS, 389, 1924
Fukugita, M., Shimasaku, K., & Ichikawa, T. 1995, PASP, 107, 945
Gavazzi, G., Boselli, A., Scodeggio, M., Pierini, D., & Belsole, E. 1999, MNRAS, 304, 595
Gavazzi, G., Boselli, A., Donati, A., Franzetti, P., & Scodeggio, M. 2003, A&A, 400, 451
Geha, M., Guhathakurta, P., & van der Marel, R. P. 2002, AJ, 124, 3073
Geha, M., Guhathakurta, P., & van der Marel, R. P. 2003, AJ, 126, 1794
Gil de Paz, A., Boissier, S., Madore, B. F., et al. 2007, ApJS, 173, 185
Giovanelli, R., & Haynes, M. P. 2002, ApJ, 571, L107
Giovanelli, R., Haynes, M. P., da Costa, L. N., et al. 1997a, ApJ, 477, L1
Giovanelli, R., Haynes, M. P., Herter, T., et al. 1997b, AJ, 113, 22
González, J. J. 1993, PhD Thesis, Thesis University of California, Santa Cruz, Source: Dissertation Abstracts International, Volume: 54-05, Section: B, 2551
Kormendy, J., & Bender, R. 1996, ApJ, 464, L119+
Kormendy, J., Fisher, D. B., Cornell, M. E., & Bender, R. 2009, ApJS, 182, 216
Le Borgne, D., Rocca-Volmerange, B., Prugniel, P., et al. 2004, A&A, 425, 881
Lisker, T., Glatt, K., Westera, P., & Grebel, E. K. 2006a, AJ, 132, 2432
Lisker, T., Grebel, E. K., & Binggeli, B. 2006b, AJ, 132, 497
Lisker, T., Grebel, E. K., Binggeli, B., & Glatt, K. 2007, ApJ, 660, 1186
Mastropietro, C., Moore, B., Mayer, L., et al. 2005, MNRAS, 364, 607
Mei, S., Blakeslee, J. P., Côté, P., et al. 2007, ApJ, 655, 144
Michielsen, D., Boselli, A., Conselice, C. J., et al. 2008, MNRAS, 385, 1374
Moore, B., Lake, G., & Katz, N. 1998, ApJ, 495, 139
Paturel, G., Petit, C., Prugniel, P., et al. 2003, A&A, 412, 45
Paudel, S., Lisker, T., Kuntschner, H., Grebel, E. K., & Glatt, K. 2010, MNRAS, 570
Pedraz, S., Gorgas, J., Cardiel, N., Sánchez-Blázquez, P., & Guzmán, R. 2002, MNRAS, 332, L59
Peletier, R. F., Davies, R. L., Illingworth, G. D., Davis, L. E., & Cawson, M. 1990, AJ, 100, 1091
Persic, M., Salucci, P., & Stel, F. 1996, MNRAS, 281, 27
Prugniel, P., Soubiran, C., Koleva, M., & Le Borgne, D. 2007, unpublished [`arXiv:astro-ph/0703658`]
Sánchez-Blázquez, P., Peletier, R. F., Jiménez-Vicente, J., et al. 2006, MNRAS, 371, 703
Sánchez-Janssen, R., Méndez-Abreu, J., & Aguerri, J. A. L. 2010, MNRAS, 406, L65
Sandage, A., Binggeli, B., & Tammann, G. A. 1985, AJ, 90, 1759
Sargent, W. L. W., & Turner, E. L. 1977, ApJ, 212, L3
Schlegel, D. J., Finkbeiner, D. P., & Davis, M. 1998, ApJ, 500, 525
Silich, S., & Tenorio-Tagle, G. 2001, ApJ, 552, 91
Simien, F., & Prugniel, P. 2002, A&A, 384, 371
Toloba, E., Boselli, A., Gorgas, J., et al. 2009, ApJ, 707, L17
Tonry, J. L., Dressler, A., Blakeslee, J. P., et al. 2001, ApJ, 546, 681
van Zee, L., Barton, E. J., & Skillman, E. D. 2004a, AJ, 128, 2797
van Zee, L., Skillman, E. D., & Haynes, M. P. 2004b, AJ, 128, 121
Vazdekis, A., Sánchez-Blázquez, P., Falcón-Barroso, J., et al. 2010, MNRAS, 404, 1639
White, S. D. M., & Frenk, C. S. 1991, ApJ, 379, 52
White, S. D. M., & Rees, M. J. 1978, MNRAS, 183, 341
Wolf, J., Martinez, G. D., Bullock, J. S., et al. 2010, MNRAS, 406, 1220
York, D. G., Adelman, J., Anderson, Jr., J. E., et al. 2000, AJ, 120, 1579
Yoshii, Y., & Arimoto, N. 1987, A&A, 188, 13
Zaritsky, D., Gonzalez, A. H., & Zabludoff, A. I. 2006, ApJ, 638, 725

Pages 15 to 24 are available in the electronic edition of the journal at `http://www.aanda.org`

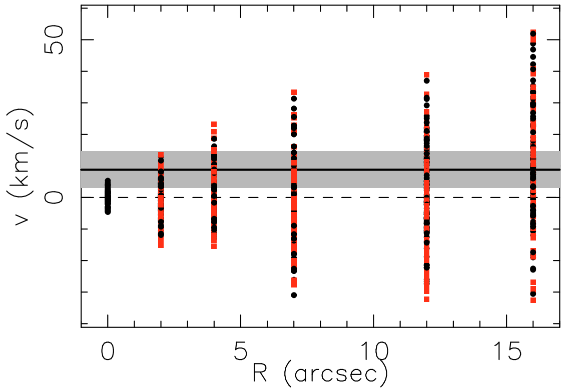

Fig. A.1. Simulations performed to quantify the bias that can be introduced in the measurement of $v_{\max}$. Plotted are the 100 folded rotation curves computed with random numbers distributed as a Gaussian with width the typical errors of the target galaxies for that radius. Red squares and black dots are the left and right arms of the unfolded rotation curves, respectively. The thick black line is the mean $v_{\max}$ for all the simulations. The grey shaded area is the scatter for this mean.

Appendix A: Quantification of the bias introduced in $v_{\max}$

Using the technique described in Sect. 5.2 to measure the maximal rotation speed, it seems that none of the galaxies have zero rotation (look at the $v_{\max}$ presented in Table 4). However, rotation curves like PGC1154903 or VCC1087 (Fig. 6) appear to be statistically consistent with no rotation. That we always find positive maximum velocities is a consequence of the method used to measure it. To quantify the bias introduced by this technique, we ran some simulations. We took a zero-rotation object with errors typical of those galaxies that statistically are non-rotators. We took a typical rotation curve with 11 bins, at 0, 2″, 4″, 7″, 12″, and 16″, with symmetrical errors of 2, 5, 7, 10, 12, and 15 km s^{-1} respectively. From these errors we generated 100 simulated rotation curves assigning to each radius a random number with a Gaussian distribution, of which the width is the error associated to that radius. After folding these simulated rotation curves, shown in Fig. A.1, we calculated $v_{\max}$ exactly following the same technique as the one we used for the target galaxies. We then obtained a mean value for the 100 values of $v_{\max}$ and its scatter, 9 ± 6 km s^{-1}, shown as a thick black line and a grey shaded area in Fig. A.1. As a result, we consider that those galaxies with $v_{\max} < 9$ km s^{-1} are not rotating, based on our data. For the other galaxies the rotation is significant (three times the standard deviation, except for VCC1122 and VCC1261, see Table 4, 3rd column), so that the systematic bias described here is much less relevant. For VCC1122 (17.3 ± 7.7 km s^{-1}) and VCC1261 (13.9 ± 5.2 km s^{-1}), the rotation is marginal, as also shown by their low $v_{\max}/\sigma$.

Appendix B: Absolute *I* band magnitudes, optical and half-light radii, and ellipticity

The *I*-band images for our sample of 21 dwarf galaxies were drawn from the Sloan Digital Sky Survey (SDSS, York et al. 2000) data release 6 (DR6 Adelman-McCarthy et al. 2008) and converted to the Johnson-Cousins system following Appendix C. The photometric parameters were calculated using the IRAF task ELLIPSE.

To remove the stars from the images, we used the IRAF task FIXPIX. This task allows us to remove the stars interpolating the surrounding galaxy area. To improve the final outcome, we averaged the results of interpolating along the horizontal and vertical directions for each star. For those galaxies that were on the edge of the FITS images or had a very bright nearby star, a more careful procedure was implemented. Taking advantage of the fact that the galaxies are ellipticals, so that they have smooth and axisymmetric surface brightness profiles, the BMODEL task of IRAF can be used to replace the affected areas of the galaxy by the azimuthal average of the unaffected ones. The output from BMODEL was only used to replace a small fraction of pixels, so this procedure was not affected by the possible presence of more subtle features, such as bars or spiral arms, which could not be reproduced by the model provided by the BMODEL task. Once extremely bright nearby stars had been removed, the same procedure as above was followed with ELLIPSE and FIXPIX.

The procedure followed to run ELLIPSE depends on the parameters we want to measure. First of all we ran ELLIPSE by fixing only the centre of the galaxy and assuming a step between isophotes of 1 pixel, while the rest of the parameters were left free. We also made the masks for the stars to be removed as described above. With the aim of measuring the absolute magnitude, $R_{\rm opt}$ and $R_{\rm eff}$ we ran ELLIPSE, again fixing the centre of the galaxy, the ellipticity, and the position angle (PA) to avoid overlap between consecutive isophotes. The adopted ϵ and PA in this case are the typical values in the outer parts of the galaxy (beyond 1.5–2$R_{\rm eff}$, region where these two parameters stabilise). To measure ϵ and C_4 we again ran ELLIPSE after removing the stars, leaving only the centre of the galaxy fixed.

Asymptotic magnitudes and the radii were derived as in Gil de Paz et al. (2007). We first computed the accumulated flux and the gradient in the accumulated flux (i.e., the slope of the growth curve) at each radius, considering the major-axis value provided by ELLIPSE as radius. After choosing an appropriate radial range, we performed a linear fit to the accumulated flux as a function of the slope of the growth curve. The asymptotic magnitude of the galaxy was the *Y*-intercept or, equivalenly, the extrapolation of the growth curve to infinity. Once the asymptotic magnitude was known, the optical and effective radii of each galaxy were obtained as the major axis of an elliptical isophote containing 83% and 50% of the total flux respectively. Different sources of error have been considered for the asymptotic magnitudes (see Appendix C). The resulting uncertainty is ~0.02 mag.

The ellipticities (ϵ) were measured as the mean value between 3″ and the $R_{\rm eff}$, the galaxy region covered by our spectroscopic observations.

Appendix C: Errors in magnitudes

The zero points (ZP) and the errors in the *i*-band magnitudes were computed as described in SDSS documentation. The ZP were obtained from F_0, which is the flux that a source produces in counts per second in the image. It is calculated as a function of three parameters (*aa*, *kk*, and airmass) and defined as

$$F_0 = \frac{t_{\rm exp}}{10^{0.4(aa+kk\times{\rm airmass})}}, \tag{C.1}$$

where the exposure time ($t_{\rm exp}$) is the same for all the SDSS images (53.91 s). The uncertainties in the *i*-band magnitudes are affected by different sources of error: firstly, the errors in the flux, that can be calculated following the equation

$$\Delta F = \sqrt{\frac{F + sky}{gain} + N_{\rm pix}({\rm dark\ variance} + \Delta sky)} \tag{C.2}$$

where F is the total flux in counts, the *sky* and Δsky are the background sky and its error (in counts), the *gain* and the *dark variance* are given in the header, and $N_{\rm pix}$ is the number of pixels in the largest aperture where the flux is measured. This error was typically 10^{-3} mag. Other error sources are the error introduced in the fit to the growth curve (between 10^{-3} mag and 6×10^{-3} mag), and the error due to photometric zero point differences between the different scans of SDSS, which might lead to an error of 0.01 mag. SDSS i-band magnitudes are not exactly in the AB system, so an error of 0.01 mag might also be introduced (see SDSS documentation about the photometric flux calibration). And finally, we transformed our data from the SDSS i-band to the Johnson-Cousins I-band assuming $m_I = m_i - 0.52 \pm 0.01$ mag Fukugita et al. (1995) given that their $r - i$ colour ranges from 0.23 mag to 0.57 mag.

After adding all these sources of error quadratically, the final estimated error is 0.02 mag for the apparent I-band magnitudes.

Appendix D: The C_4 boxyness/diskyness parameter

The boxyness/diskyness parameter is defined as the fourth moment in the Fourier series as follows

$$I(\Phi) = I_0 + \sum_k [S_k \sin(k\Phi) + C_k \cos(k\Phi)], \tag{D.1}$$

where $I(\Phi)$ is the intensity measured in each isophote. The first two moments in this series completely describe an ellipse. Higher order moments ($k \geq 3$) define deviations in the isophotes from ellipses. The third-order moments (S_3 and C_3) represent isophotes with three-fold deviations from ellipses (e.g. egg-shaped or heart-shaped), while the fourth-order moments (S_4 and C_4) represent four-fold deviations. Rhomboidal or diamond shaped isophotes have nonzero S_4. For galaxies that are not distorted by interactions, C_4 is the most meaningful moment, indicating the disky/boxy shapes of the isophotes (see Fig. 1 from Peletier et al. 1990 for an example of these different shapes).

C_4 is measured in i-band SDSS images using ELLIPSE that performs equation D.1 along the radius of the galaxy fixing only the centre of the galaxy and leaving the rest of ELLIPSE parameters free, as described in Sect. 6.1. Figure D.1 shows C_4 as a function of radius for 3 dEs. In the upper panel one can see that if an average value is used between the dashed lines, C_4 will be compatible with zero and, as a consequence, the prominent disky structure will be smeared out by the adjacent regions. In contrast, in the middle panel a galaxy with no clear disky structures is shown. In this latter case the errors are larger. The bump in C_4 only covers $\sim 3''$, while the rest of the galaxy is boxy. In this situation a mean value of the C_4 and its scatter is more representative. In the lower panel VCC1695 is an example of a typical boxy shaped galaxy. Due to the usual large changes of C_4 with radii, taking an averaged value is therefore not the best way to detect disks in these galaxies, especially if they only cover a limited range in radius. We have thus adopted the following procedure.

If at least one prominent bump is detected, which has a width larger than $\sim 6''$ inside three effective radii (above this radius the scatter of C_4 and its error become too large to be reliable), we consider the galaxy to be disky and assign the maximum C_4 between $3''$ and $3R_{\rm eff}$ to the global C_4. The error in this measurement has been estimated by dividing the photometric error of the maximum of C_4 by the square root of the number of points that describe the disky structure in order to quantify the reliability of the bump considered. If the bump is described by a large number of points, it is highly likely that the bump is truly there so the error will be small, but if the number of points is small but the photometry is of high quality then the error will again be small. In any other case, the error will be large and the result must be used cautiously.

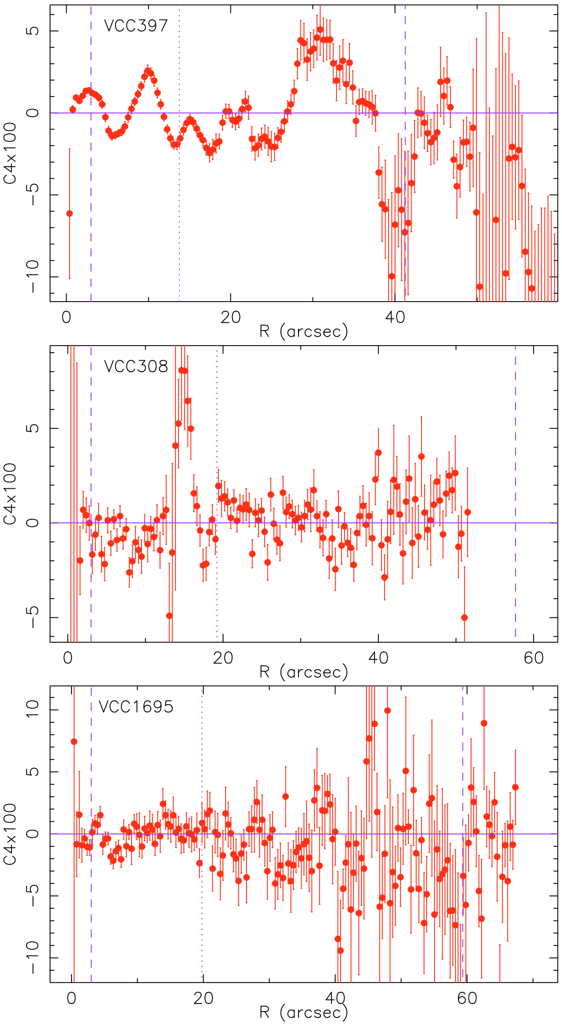

Fig. D.1. Examples of C_4 vs. radius for three galaxies: VCC397, VCC308 and VCC1695. The dashed purple lines indicate the region between $3''$ and the $3R_{\rm eff}$. The dotted purple line shows the $R_{\rm eff}$.

Otherwise, if the values oscillate around $C_4 \sim 0$ (lower panel of Fig. D.1), are always negative, or if there is a bump with a small radial coverage (see middle panel Fig. D.1), we assign a mean value and its scatter between $3''$ and $3R_{\rm eff}$ to the global C_4. In this case, the RMS quantifies the quality of the photometry simultaneously and the possible presence of small bumps (as it is the case of VCC308, middle panel of Fig. D.1).

The results obtained for this parameter are listed in Table 6 and plotted vs. the anisotropic parameter, $(v_{\rm max}/\sigma)^*$, in Fig. 10. The agreement between the C_4 classification in disky/boxy galaxies and the morphological classification from Lisker et al. (2006b) is evident but apart from three red dots. These correspond to VCC917, a rotationally supported galaxy with strong disky isophotes but no structure found by Lisker et al. (2006a); VCC1122, a dE that is not rotationally supported but that shows appreciable rotation in Fig. 6 and a significant disky structure in the inner $R_{\rm eff}$ not detected by Lisker et al. (2006a); and VCC1912, inside half the effective radius a moderate rotation is found in this system with a clear disky feature that peaks at $1.5R_{\rm eff}$. For this galaxy, however, no underlying structure was found by Lisker et al. (2006a). More importantly, VCC308 and VCC856, two rotationally supported galaxies with boxy C_4, present prominent spiral arms in Lisker et al. (2006a). In Ferrarese et al. (2006), based on ACS-HST images, VCC856 also shows spiral arms but their analysis of the isophotes' shapes shows that they are boxy too. Looking at Table 6 we see that both galaxies are nearly face-on, which means that the isophotes are boxy since face-on disks are round and not disky. As a consequence, we emphasise that boxy isophotes could miss disk features (mainly if the galaxies are face-on), but not the other way round (see VCC917).

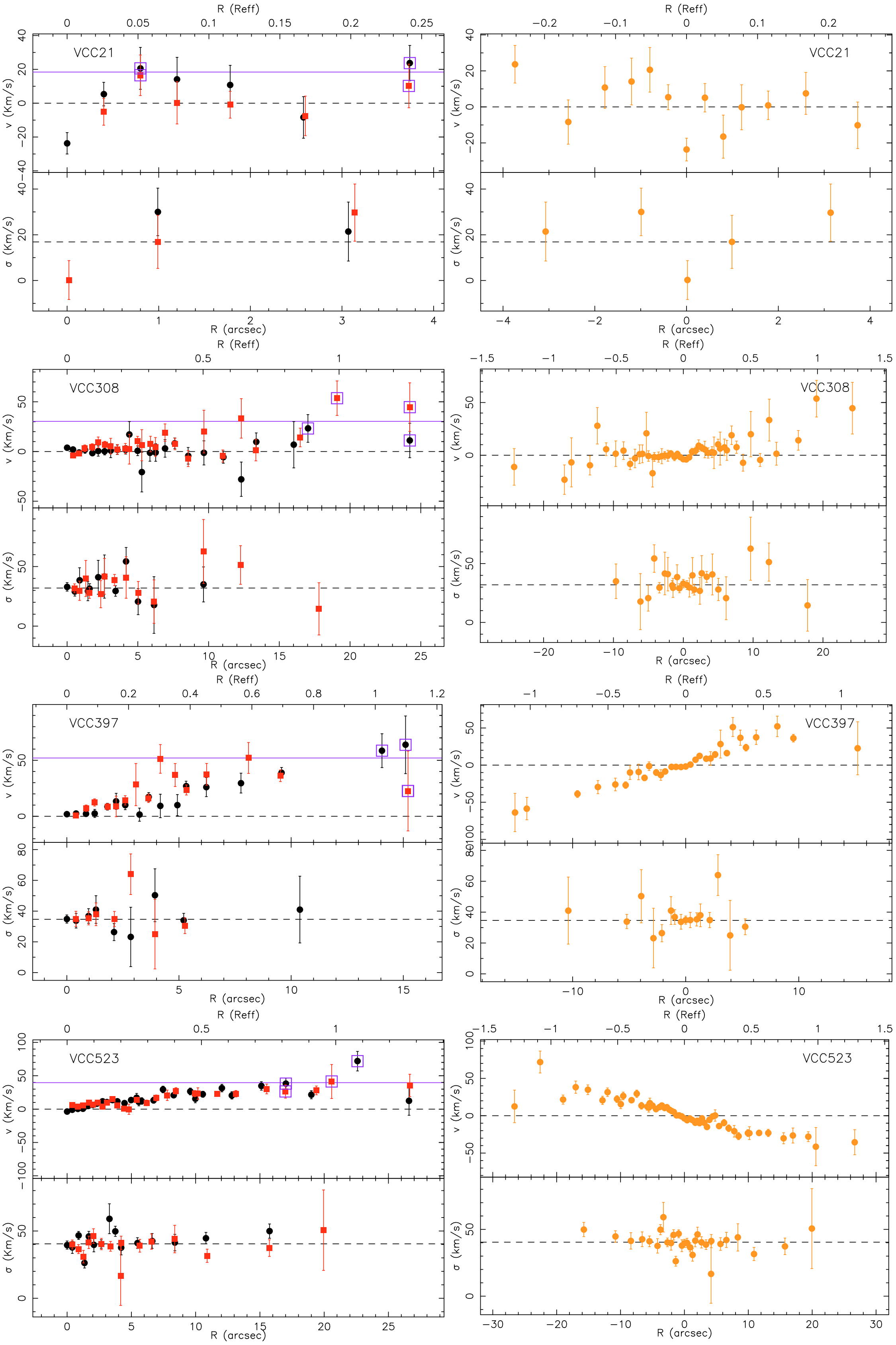

Fig. 6. continued.

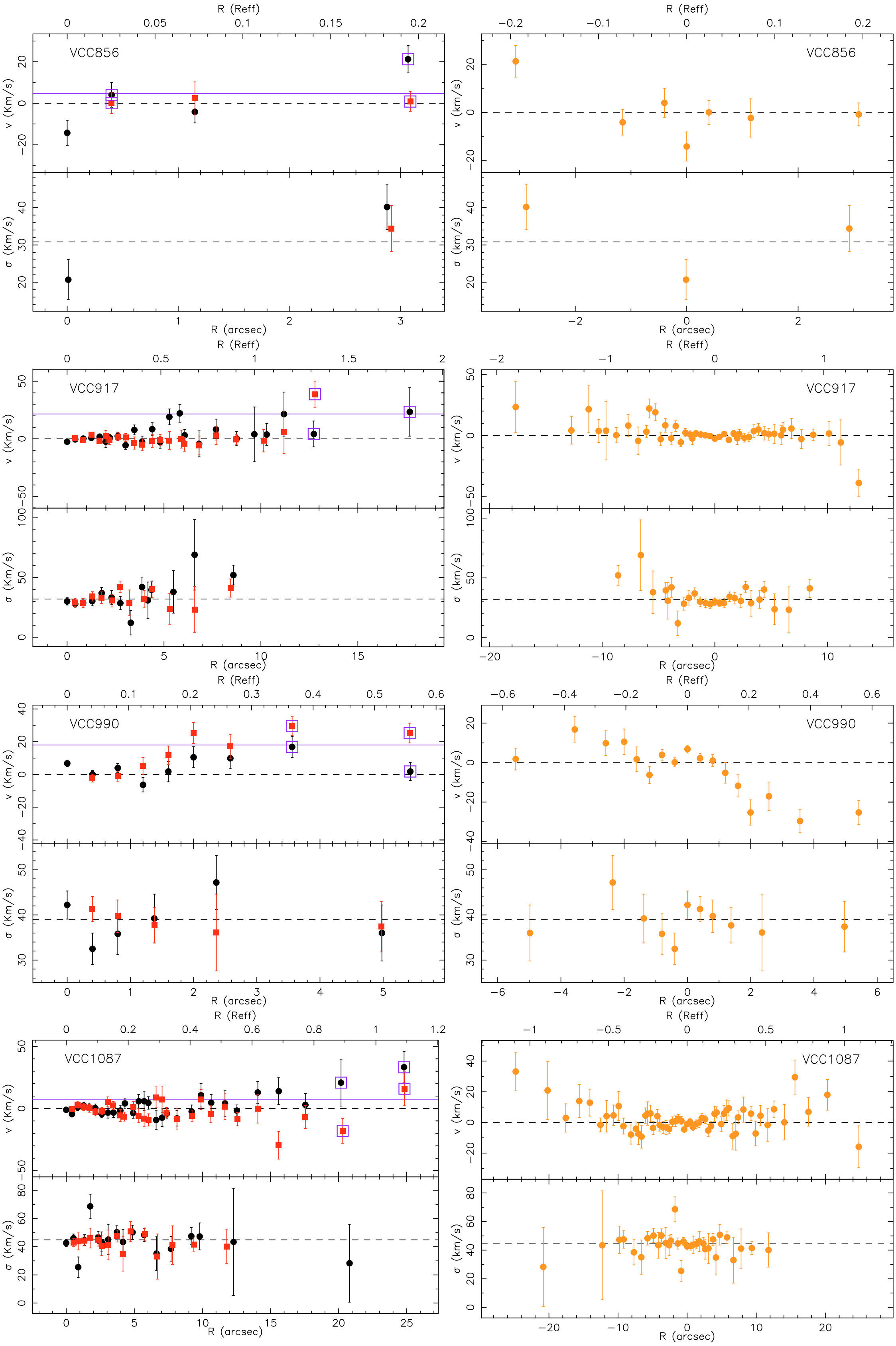

Fig. 6. continued.

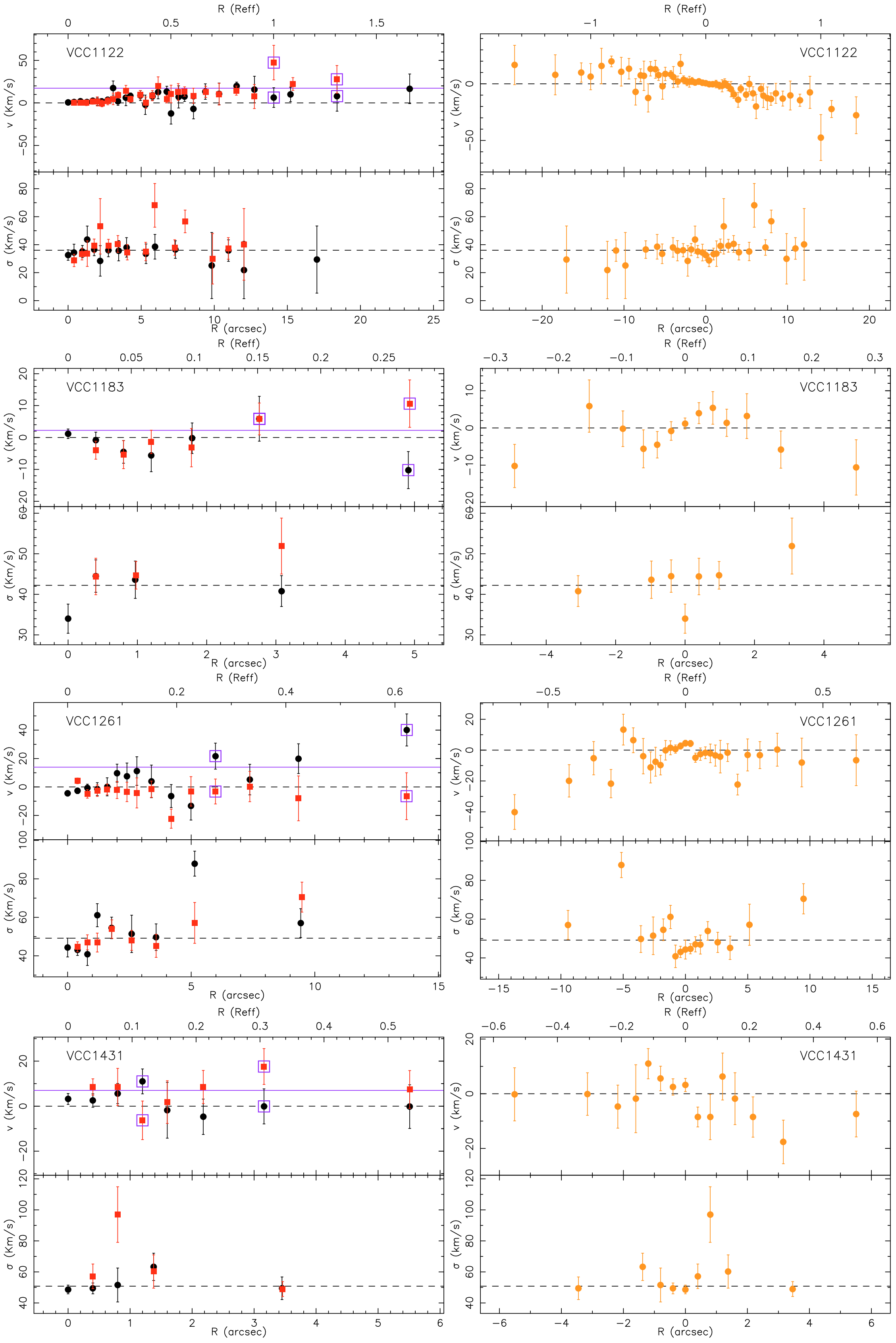

Fig. 6. continued.

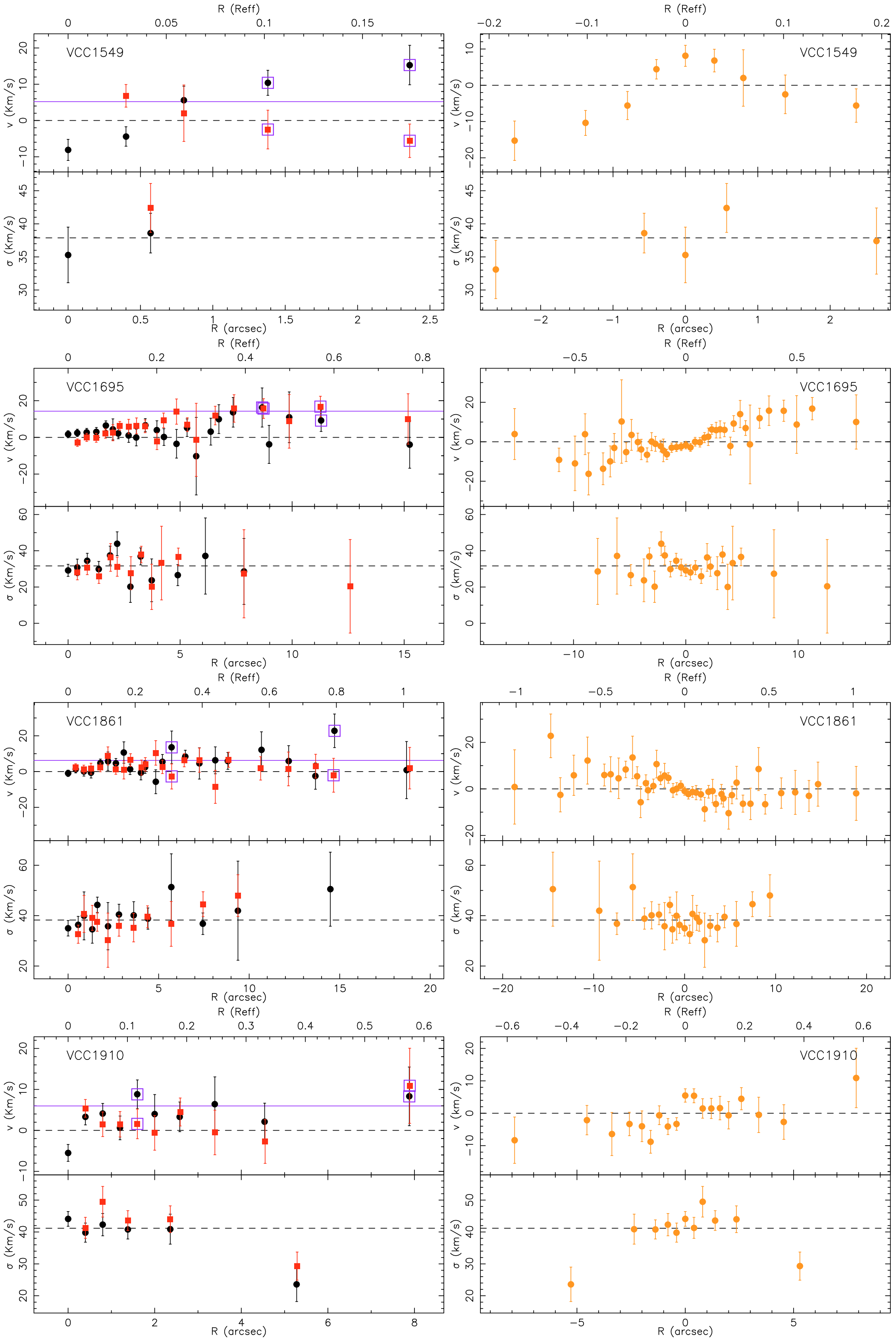

Fig. 6. continued.

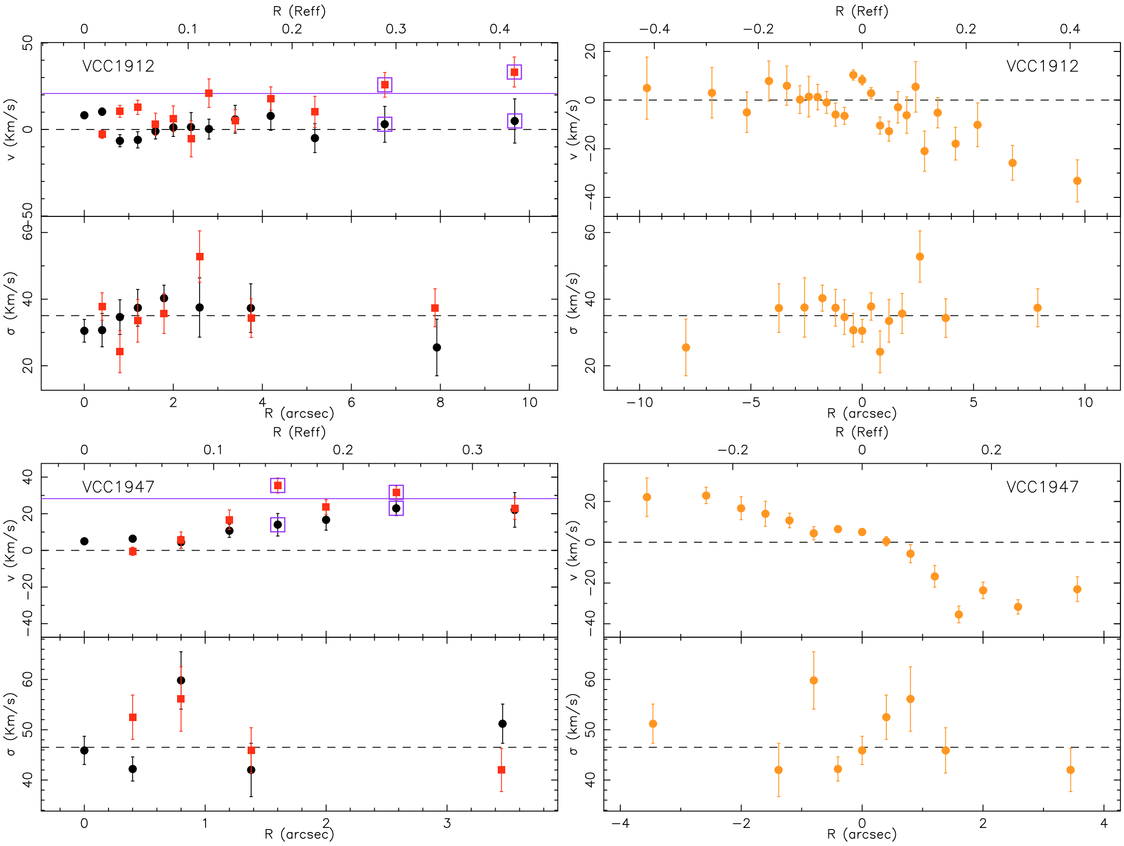

Fig. 6. continued.

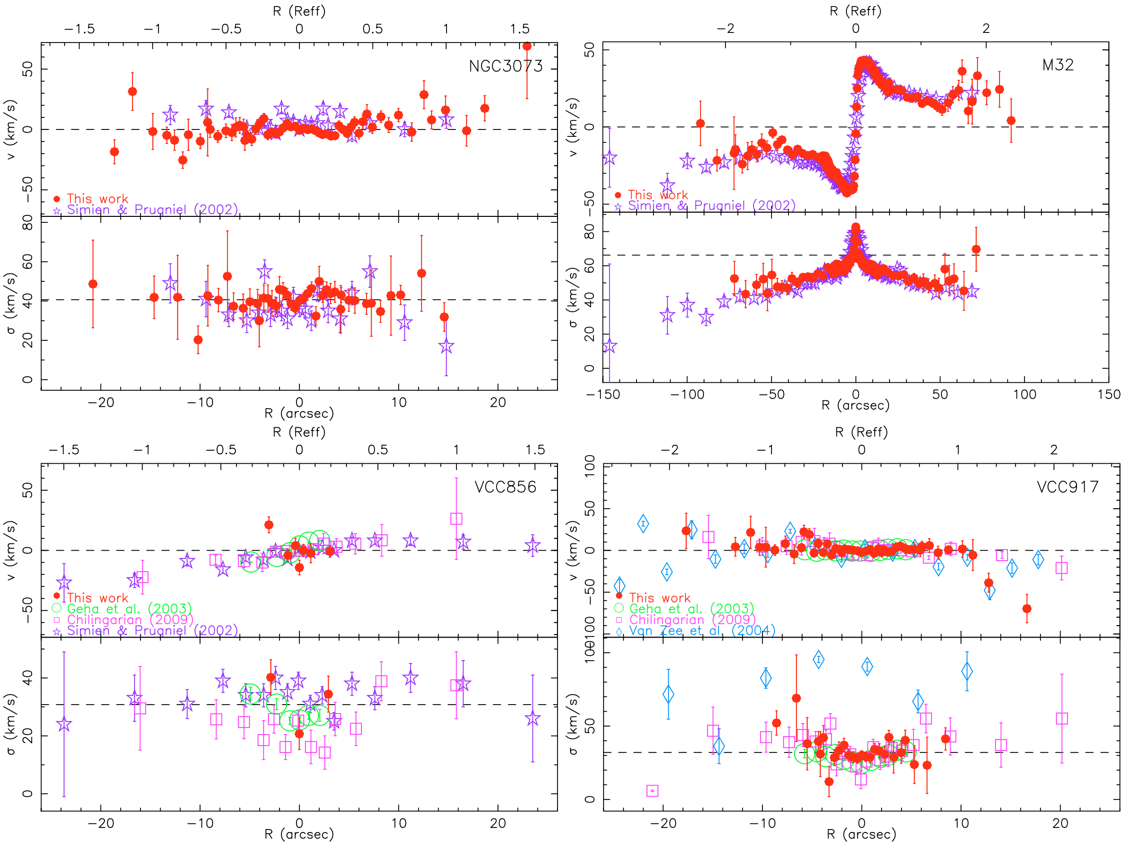

Fig. 7. Comparison of our kinematic profiles with other works. Each diagram shows the rotation curve (upper panel) and the velocity dispersion profile (lower panel). The bottom X-axis is measured in arcseconds and the upper X-axis is measured as a fraction of the effective radius ($R_{\rm eff}$) of each galaxy in i band (see Sect. 6). For Van Zee et al. (2004) we only present their velocity profiles for MgbI, more similar in wavelength to our data.

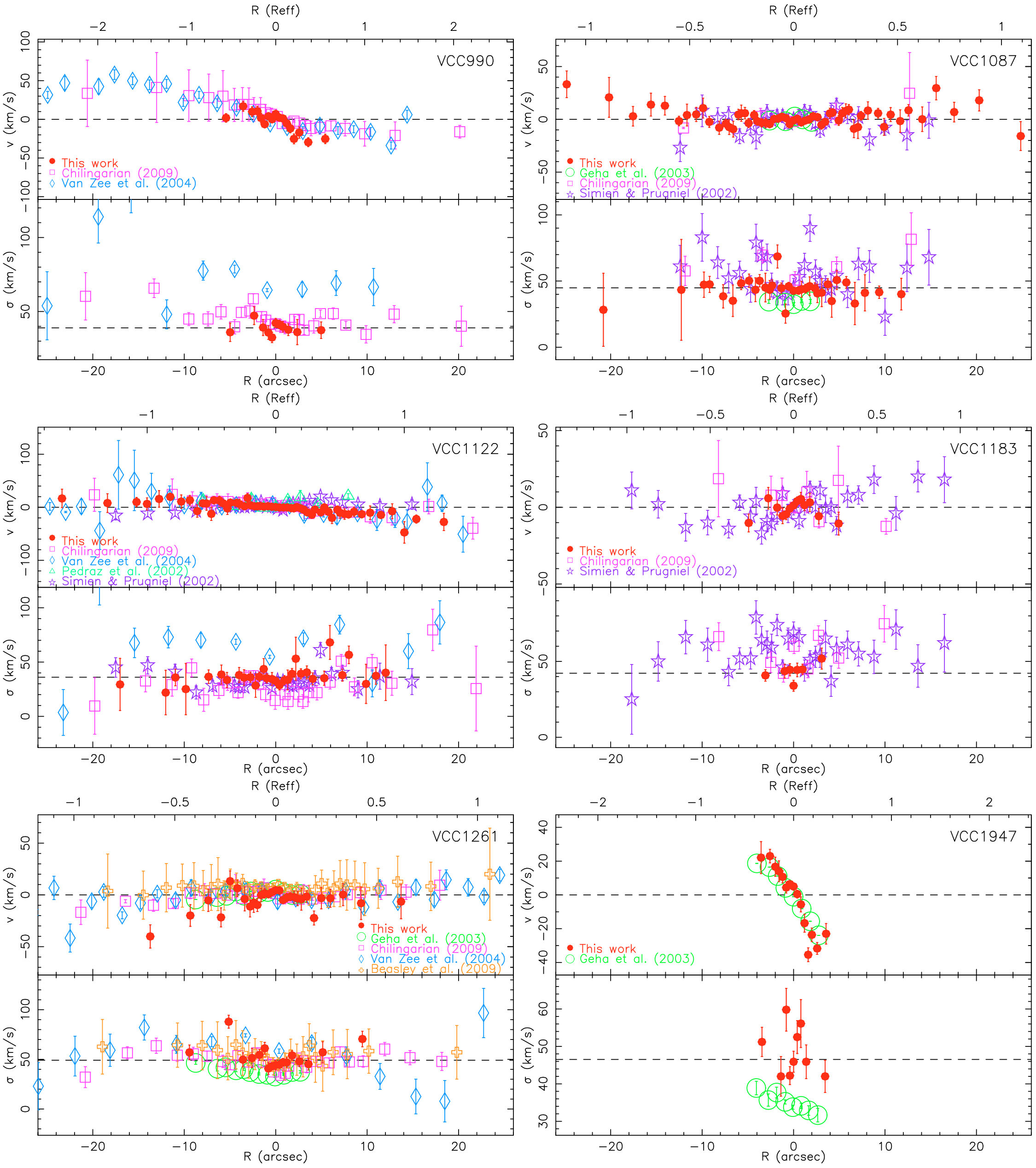

Fig. 7. continued.